Sun *et al. Biochar* (2022) 4:53
https://doi.org/10.1007/s42773-022-00177-8

Biochar

ORIGINAL RESEARCH Open Access

Formable porous biochar loaded with La-Fe(hydr)oxides/montmorillonite for efficient removal of phosphorus in wastewater: process and mechanisms

Enhui Sun[1,2*], Yanyang Zhang[3], Qingbo Xiao[1], Huayong Li[4], Ping Qu[1], Cheng Yong[1], Bingyu Wang[5], Yanfang Feng[1*], Hongying Huang[1], Linzhang Yang[1,2] and Charles Hunter[2]

Abstract

The development of biochar-based granule-like adsorbents suitable for scaled-up application has been attracting increasing attention in the field of water treatment. Herein, a new formable porous granulated biochar loaded with La-Fe(hydr)oxides/montmorillonite (LaFe/MB) was fabricated via a granulation and pyrolysis process for enhanced phosphorus (P) removal from wastewater. Montmorillonite acted as a binder that increased the size of the granulated biochar, while the use of Fe promoted the surface charge and facilitated the dispersion of La, which was responsible for selective phosphate removal. LaFe/MB exhibited rapid phosphate adsorption kinetics and a high maximum adsorption capacity (Langmuir model, 52.12 mg P g^{-1}), which were better than those of many existing granulated materials. The desorption and recyclability experiments showed that LaFe/MB could be regenerated, and maintained 76.7% of its initial phosphate adsorption capacity after four adsorption cycles. The high hydraulic endurance strength retention rate of the developed material (91.6%) suggested high practical applicability in actual wastewater. Electrostatic attraction, surface precipitation, and inner-sphere complexation via ligand exchange were found to be involved in selective P removal over a wide pH range of 3–9. The thermodynamic parameters were determined, which revealed the feasibility and spontaneity of adsorption. Based on approximate site energy distribution analyses, high distribution frequency contributed to efficient P removal. The research results provide a new insight that LaFe/MB shows great application prospects for advanced phosphate removal from wastewater.

Highlights

- Novel formable porous functional biochar (LaFe/MB) was prepared for P removal.
- La/Fe oxide provides abundant sorption sites for P and almost no La/Fe leaching.
- LaFe/MB presented high compressive strength with high sorption capacity for P.

*Correspondence: enhsun@126.com; jaasfengyanfang@163.com

[1] Key Laboratory of Saline-Alkali Soil Improvement and Utilization (Coastal Saline-Alkali Lands), Ministry of Agriculture and Rural Affairs, Jiangsu Collaborative Innovation Center for Solid Organic Waste Resource Utilization, Institute of Agricultural Resources and Environment, Jiangsu Academy of Agricultural Sciences, Nanjing 210014, China
Full list of author information is available at the end of the article

Keywords: Formable porous biochar, Montmorillonite, Metal (hydr)oxide, Wastewater phosphate removal, Adsorption mechanism

Graphical Abstract

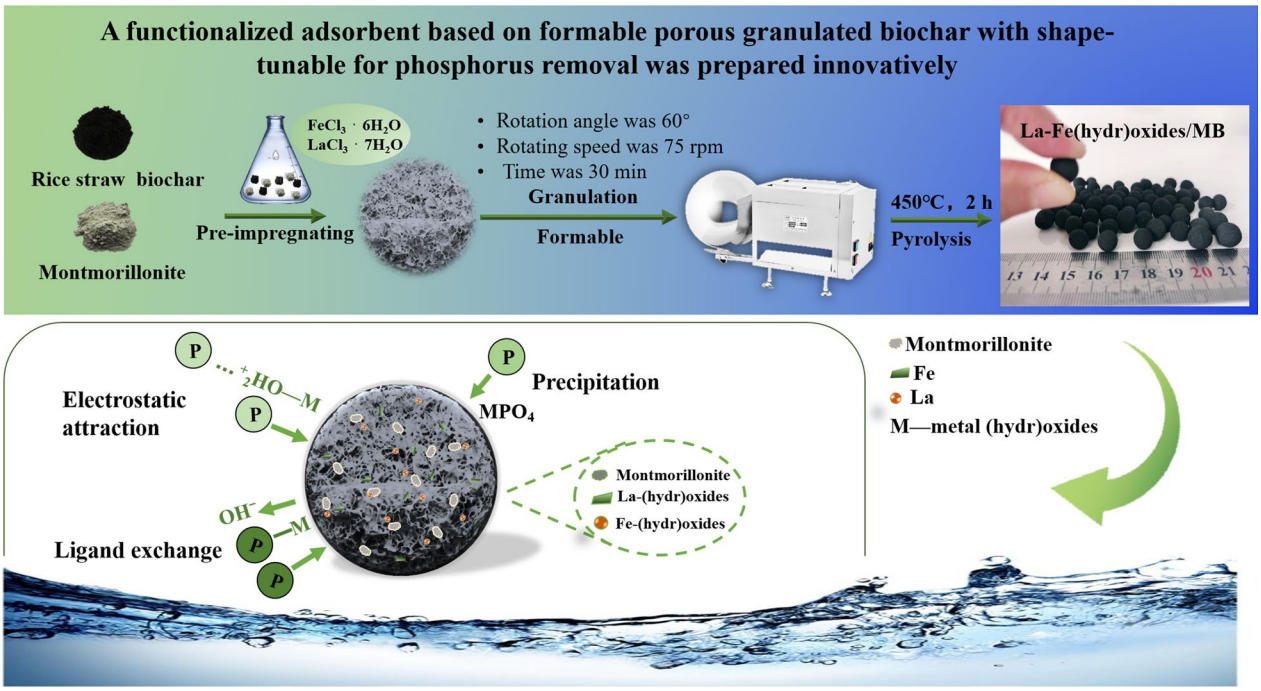

1 Introduction

Phosphorus (P) eutrophication is a growing concern globally (Cakmak et al. 2022). P is a key limiting nutrient for plant growth and essential for agricultural production (Ngatia et al. 2017); however, its contribution to underground water contamination and water bodies' eutrophication remains a major problem, which has been significantly accelerated by the intensification of agricultural activities (livestock production through fecal matter and urine; fertilizer application for crop production; manure application for crop production) and the expansion of urbanization and industrialization (Zhang et al. 2021b). As reported, algae bloom occurred even at trace level (e.g. > 0.02 mg L^{-1}) (Banu et al. 2018). This necessitates comprehensive consideration of P management options and mitigation measures in agricultural fields to achieve downstream and groundwater P reductions. Significant efforts have been made by scientists worldwide to find ways to lower the phosphate concentration in wastewater (Viglasova et al. 2018). Several techniques such as crystallization (Le Corre et al. 2009), membrane separation (Arola et al. 2021), chemical precipitation (Caravelli et al. 2012), biological (Islam et al. 2017), and adsorption (Melia et al. 2019) have been adopted to remove phosphate in wastewater. The control of phosphate levels using the adsorption method is of increasing interest due to its expected ability to realize P recovery and utilization through desorption to enhance P eutrophication mitigation (Bacelo et al. 2020). Meanwhile, in terms of possible shortage of phosphate ore, immobilization from the wastewater systems can be a promising way to supply secondary sourced P to the market, thereby promoting the blue economy (Cakmak et al. 2022).

Biochar is the carbon-rich product obtained from the thermochemical conversion of biomass under oxygen-limited conditions (Wu et al. 2019), which has become a focal point of multidisciplinary research because of its unique characteristics, broad application, and promising development prospects (Chen et al. 2019; Kumar et al. 2020a). Biochar has been used for removal of heavy metals (Wang et al. 2020a), trace organic contaminants (Rong et al. 2019), ammonium ions (Zhang et al. 2020), and especially phosphate (Bacelo et al. 2020) from wastewater due to its high surface porosity, relatively large specific surface area, surface charge (Panahi

et al. 2020; Tomczyk et al. 2020; Wu et al. 2020), and abundant functional groups (Mohan et al. 2014; Rajapaksha et al. 2016; Wang et al. 2017). However, pristine biochar usually has unsatisfactory sorption capability, and further modifications for advanced P removal of wastewater are needed (Huang et al. 2019; Viglasova et al. 2018). Researches demonstrated that $La(OH)_3$-modified canna biochar has a P removal rate of up to 99% in 37.37 mg P g^{-1} (Liu et al. 2022). A kind of lanthanum-based biochar from wheat stalks was used by Huang et al. (2022) for the removal of phosphate, exhibiting excellent adsorption capacities for P (64.3 mg g^{-1}) (Huang et al. 2022). Feng et al. (2017) reported a novel nano-cerium oxide functionalized maize straw biochar (Ce-MSB), and the application of Ce-MSB decreased the total phosphorus concentration of surface water by 27.33% (Feng et al. 2017). It was previously reported that the nanocomposite porosity-enhanced MgO/biochar (PE-MgO/biochar) assembly by a novel combined electrochemical modification (CEM) method had a maximum phosphate adsorption capacity of more than 20 mg P g^{-1} (Jung and Ahn 2016). However, biochars are usually present as ultra-fine powders, which cause blockage in adsorption columns and difficulty during recycling and reuse (Ai et al. 2019; Kumar et al. 2020b; Song et al. 2019; Xu et al. 2020a). Superior adsorption, ease of separation, and recyclability of adsorbent were crucial for application in an actual engineering environment (Weber and Quicker 2018).

Formable methods can significantly increase the size of the biochar to a granular scale, hence improving the hydraulic properties of biochar, so that they can be separated, recovered and reused. Recently, $MgFe_2O_4$-BM-La was synthesized via co-precipitation of iron and magnesium onto a reed biomass precursor, followed by crosslinking with lanthanum alginate. The resulting material showed the highest phosphate adsorption capacity, 2.5 times higher than that of BM-La and $MgFe_2O_4$-La. The capacity loss was only about 30% after three consecutive adsorption-regeneration cycles in the fixed bed column operation (Wang et al. 2020b). Jung et al. (2016) prepared granular biochar with calcium-alginate, which exhibited better performance than other powder adsorbents. In general, these granular biochar materials obtained by the formable method showed enhanced phosphate removal capability and hydraulic properties compared to their powder counterparts, making them promising candidates for column-based phosphate adsorption technology (Jung et al. 2016).

Clay minerals are also important materials for contaminant immobilization (An et al. 2020; Lazaratou et al. 2020). More importantly, the viscous montmorillonite can improve the diameter of biochar, which is beneficial to the recovery and separability of adsorbent (Vieira et al. 2018; Yao et al. 2014). Previous literature reported the preparation of montmorillonite-biochar composites (MBC) by the co-pyrolysis of montmorillonite and bamboo powder. MBC showed a maximum adsorption capacity of 34.72 mg P g^{-1} for PO_4^{3-} by the Langmuir model, which was attributed to the electrostatic attraction or ionic bonding between PO_4^{3-} and cations in the MBC samples such as Ca^{2+}, Mg^{2+}, Al^{3+}, and Fe^{3+} (Chen et al. 2017). Additionally, exchangeable cations in the interlayer of montmorillonite, including Fe^{2+}, Ca^{2+}, and Mg^{2+}, can balance the negative charges, thus effectively enhancing the active adsorption sites (Arif et al. 2021). In fact, a variety of surface-modified biochar-clay composites were synthesized using hematite as a modifier and granulated into ~ 4 mm grains by a mixer granulator for water treatment processes (Zhu et al. 2020). However, the efficient performance of adsorbents still presents significant challenges.

Oxides composed of multiple metals generally exhibit significantly superior physicochemical properties to single-component oxides. Several polymetallic oxides have been developed and used to improve phosphorus removal (Delaney et al. 2011; Shi et al. 2019). In recent years, various metal oxides or hydroxides, especially Fe^{2+}, La^{2+}, and Mg^{2+}, have been reported in-depth. In previous literature, it was found that magnetite/lanthanum hydroxide [M-$La(OH)_3$] hybrids adsorbed 52.7 mg P g^{-1} (Fang et al. 2018), while ferrihydrite-coated, lanthanum-decorated magnetite absorbed 44.8 mg P g^{-1} (Fu et al. 2018). In addition, lanthanide compounds showed strong ligand adsorption for phosphate even at trace levels due to their strong lewis acidity and multi-point coordination ability (Qiu et al. 2017). Moreover, a study suggested that the introduction of iron can promote the uniform distribution of lanthanum iron bimetallic oxides in the Fe_3O_4/$La(OH)_3$ nanocomposite matrix (Ahmed and Lo 2020). Based on the above background, lanthanum and iron can be co-loaded onto biochar to prepare low-cost composites with uniformly dispersed bimetallic oxides, which would be a promising phosphate removal adsorbent.

Pelletizing is a common technology to increase the particle size of powder adsorbent. Montmorillonite is a low-cost, non-toxic, and environmentally friendly viscous adsorbent material that not only provides metal oxides but also provides strong bonding and forming properties. Through impregnating the surfaces of biochar and montmorillonite with iron and lanthanum metal ions, the content of metal colloidal oxides and active adsorption sites on the surface of the mixed adsorption material can be increased. This can further improve the adsorption capacity of phosphorus as well as the granulation of biochar.

Herein, a method was developed for preparing a novel formable porous granulated straw biochar-loaded La-Fe (hydr)oxides/montmorillonite (LaFe/MB) adsorbent, in which iron and lanthanum bimetallic oxides are immobilized in micro-meter sized biochar granulated with montmorillonite. The structure of the modified biochar was systematically characterized. The adsorption process of phosphate from wastewater by LaFe/MB was described by mathematical models, including adsorption kinetics and isotherms, and the possible adsorption mechanisms were proposed. Furthermore, site energy distribution (SED) is a useful method in treating complex adsorption issues. SED analysis provides direct and detailed information on how tight of the binding energy between adsorbate and adsorbent (Li et al. 2021). Site energy model also reveals the distribution of valid adsorption sites, and it is essential for why a good performance can be achieved by some adsorbents (Shen et al. 2015). We comprehensively analyzed the adsorption mechanism via a combination of SED and characterization analysis, and proposed the foremost adsorption mechanism for the adsorbent. The use of LaFe/MB not only effectively enhances the relief of P eutrophication, but also realizes the efficient immobilization recovery of P resources. Therefore, analyzing and mining such kind of data is of great significance for advancing many scientific problems and real engineering applications.

2 Materials and methods

2.1 Materials

Rice straw residue was provided by Jiangsu Academy of Agricultural Sciences (Nanjing, China) (34°15′29.99″ N, 108°55′43″ E). Before use, it was air-dried, crushed, and sieved to 2–5 mm mesh size. Dried straw samples were placed in a porcelain crucible and pyrolyzed for 2 h at 550 °C in a rotating tube furnace (RTL 1200, Nanjing Boyuntong Instrument Technology CO., LTD.) under N_2 atmosphere (Fletcher et al. 2013; Yang et al. 2016). Straw biochar (B) was crushed and passed through a 0.42 mm stainless steel sieve. Nano-montmorillonite particles (M) were obtained from Huzhou New Material Co., Ltd., China. Iron(III) chloride hexahydrate ($FeCl_3{\cdot}6H_2O$, 97%) and lanthanum(III) chloride heptahydrate ($LaCl_3{\cdot}7H_2O$, 64.5–70.0%, $LaCl_3$ basis) were supplied by Sigma-Aldrich (Shanghai, China). All reagents used in this study were of analytical grade, including KH_2PO_4, HCl, and NaOH, and were purchased from Nanjing Chemical Reagent CO., LTD (Nanjing, China). All solutions required for the test were prepared with deionized water.

2.2 Preparation of formable porous granulated biochar adsorbents

A series of formable porous granulated adsorbents was prepared using the coprecipitation method. Different amounts of lanthanum chloride were added during preparation to obtain Fe^{3+}: La^{3+} molar ratios of 0.4:0, 0.3:0.1, 0.2:0.2, 0.1:0.3, and 0:0.4. Preparation conditions for all adsorbents are summarized in Additional file 1: Table S1.

Briefly, finely crushed rice straw biochar was mixed with montmorillonite in a mass ratio of 2:1 using a mortar. Series of iron/lanthanum chloride solution were prepared by dissolving $FeCl_3{\cdot}6H_2O$/$LaCl_3{\cdot}7H_2O$ in 850 mL of deionized water. Among them, Fe^{3+} and La^{3+} molar ratios were 0.4:0–0:0.4, the ratio of-specific expressed as above, and controlling the total moles of metal ions was 0.4. Then, a stable mud was prepared by adding 150 g of montmorillonite/biochar composites to the series of iron/lanthanum chloride solution with pH tuned to 9.5–10 by proper amount of NaOH. Afterward, the mixtures were vigorously stirred for 30 min of impregnation in an impregnating tank (HATLAB, Shanghai Huotong Experimental Instrument CO., LTD.), and transferred into an icing machine (BY-400, Changsha Zhuocheng Medical Equipment CO., LTD.), with a rotation angle of 60° and rotating speed of 75 rpm for 30 min. Subsequently, 1–4 mm spherical composite precursors were obtained via a semi-wet granulation process, then oven-aged (60 °C) for 10 h. Finally, the precursors were calcined in a tube furnace at 450 °C for 2 h under the protection of N_2 atmosphere. The washed modified biochar was dried at 80 °C for 1 day to obtain the formable porous granulated biochar (LaFe/MB), which was labeled as $Fe_{0.4}$/MB, $La_{0.1}Fe_{0.3}$/MB, $La_{0.2}Fe_{0.2}$/MB, $La_{0.3}Fe_{0.1}$/MB, and $La_{0.4}$/MB (the number denoted the molar ratios of Fe^{3+} and La^{3+}).

2.3 Macroscopic phosphate adsorption experiments

To determine the phosphate adsorption performance, batch adsorption tests were conducted by mixing 0.2 g adsorbent with 100 mL phosphate solution (100 mg P L^{-1}) in a 250 mL conical flask (Qiu et al. 2017). The flasks were shaken at 28 °C in an oscillating incubator (THZ-98C, Shanghai Yiheng Scientific Instrument Co., Ltd., Shanghai, China) for 6 h at 180 rpm. The suspension was filtered with a 0.45 μm membrane filter and the residual concentration of phosphate aqueous solution was determined by ascorbic acid method using a UV–Vis Lightwave II spectrophotometer (Delaney et al. 2011). All experiments were performed three times for data analysis.

Kinetic tests were performed using 2 g L^{-1} of LaFe/MB with 100 mg P L^{-1} solution, shaken at 28 °C and 180 rpm for 6 h. At predetermined time intervals (0 min,

1 min, 2 min, 3 min, 5 min, 15 min, 30 min, 1 h, 2 h, 4 h, 6 h), 1 mL of the suspension was taken out to analyze the phosphate concentration, as described above. The adsorption rate was evaluated by fitting kinetic data using the pseudo-first-order model, pseudo-second-order model, and the intra-particle diffusion models (Additional file 1: Text S1) (Haris et al. 2022).

Isotherm tests were performed by adding 0.2 g LaFe/MB to 100 mL of phosphate solutions with varying initial concentrations (1.75–300 mg P L^{-1}). The adsorption capacity was determined and the equilibrium data were fitted to Langmuir and Freundlich isotherm models (Additional file 1: Text S2) as described in the literature (Qiu et al. 2017). Meanwhile, we further studied the site energy distribution deduced from the Langmuir model based on an assumption of the distribution of site energies (Reguyal and Sarmah, 2018; Wang et al. 2022). See the Additional file 1: Text S3 for details.

The effect of solution pH was assessed at pH values varying between 2 and 10 adjusted with 0.2 mol L^{-1} NaOH or HCl solution. The initial phosphate concentration was 100 mg P L^{-1} with the adsorbent dosage of 2 g L^{-1}. Experiments were conducted at 28 °C for 24 h.

The influence of competitive ions on phosphate adsorption experiment was investigated using sulfate (SO_4^{2-}), bicarbonate (HCO_3^-), chlorine (Cl^-), and nitrate (NO_3^-) at the concentrations of 50 and 100 mg L^{-1}, respectively. The experiment conditions were similar to those of the above isothermal adsorption process, except that the pH of the system was normalized to 7.4 ± 0.2.

2.4 Regeneration and recyclability experiments

The recyclability of the adsorbent was tested by four successive phosphate adsorption/desorption cycles. Phosphate desorption tests were carried out by soaking LaFe/MB in 0.1 mol L^{-1} NaOH aqueous solution. After phosphate adsorption and desorption, the adsorbent was separated from the mixture. Then, it was washed to neutral with deionized water and dried at 60 °C before the start of the next cycle.

2.5 Strength retention rate and pressure resistance tests

The damage to the skeleton and surface of adsorbents after the mechanical wear was analyzed. The grain percentage was used as the sample strength indicator according to GB/T 12496.6-1999. The adsorbents with the same diameter were placed on the mold. A microcomputer-controlled electronic universal testing machine (HY-0580, Shanghai Hengyi Precision Instrument CO., LTD., Shanghai) was adopted. The pressure resistance was measured at 28 °C and the speed of applied loading was set at 10 mm min^{-1}.

2.6 Analysis methods

The specific surface area and pore structure of the adsorbents were determined using an automatic adsorption instrument (USA, ASAP2020) and calculated using the BET adsorption isotherm of nitrogen (77 K). The functional groups of adsorbents were assessed using Fourier transform infrared spectroscopy (Tensor27, Bruker, Germany). X-ray diffraction (XRD, DX-2000, Darmstadt, Germany) with Cu Kα radiation (40 kV, 20 mA) was used to detect the crystallographic phases of the adsorbent before and after adsorption. Micromorphological characteristics and surface elemental composition of adsorbents were characterized using scanning electron microscopy (SEM, FEIQUANTA200, Hillsboro, USA) coupled with energy dispersive X-ray spectroscopy (EDS, Oxford Instruments Link ISIS). The pH was determined using a PHS-3C precision pH meter (China, Changzhou). Zeta potentials were measured at different pH values to determine the zero charge point (pH_{PZC}) of the adsorbents. Raman imaging (DXR2xi, Thermo Scientific, USA) was performed to analyze the structure and composition of the adsorbent. Surface chemistry of LaFe/MB before and after phosphate adsorption was analyzed by X-ray photoelectron spectroscopy (XPS, PHI 5000 VersaProbe ESCA).

The amount of phosphate adsorbed was expressed as mean ± standard error. Experimental data were analyzed with SPSS software (SPSS, 26.0, IBM, USA), and Origin 8.5 (Origin, OriginLab, USA) was used for graphing.

3 Results and discussion

Surface modification with La^{3+} and Fe^{3+} significantly improved the phosphate removal performance of modified biochar. The phosphate adsorption capacities of the different adsorbents are presented in Additional file 1: Fig. S1. The adsorption of phosphate increased with the increase in the La^{3+}: Fe^{3+} molar ratio. However, when the molar ratio was more than 0.3:0.1, the adsorption capacity began to decrease. As shown in Additional file 1: Fig. S1, $La_{0.3}Fe_{0.1}$/MB showed the best phosphate uptake of 39.45 mg P g^{-1}, while $La_{0.2}Fe_{0.2}$/MB and $La_{0.4}$/MB exhibited weaker adsorption capacities of 30.23 and 36.38 mg P g^{-1}, respectively. This may be due to the effect of Fe^{3+} doping on the formation of lanthanum oxide, which can not only promote the dispersion of lanthanum oxide but can also enhance the surface charge of the adsorbent (Shi et al. 2019). Thus, $La_{0.3}Fe_{0.1}$/MB was selected for the following in-depth studies.

3.1 Characterization of adsorbents

The physicochemical properties of biochar (B), biochar/montmorillonite (MB), and $La_{0.3}Fe_{0.1}$/MB are

Table 1 Physicochemical properties of biochar (B), biochar/montmorillonite (MB), and $La_{0.3}Fe_{0.1}$/MB

Characteristics	B	MB	$La_{0.3}Fe_{0.1}$/MB
Particle size (mm)	< 0.3–0.45	0.3–0.45	1–45
Packing density (g mL^{-1})	0.386	0.413	0.518
S_{ssa}[a] (m^2 g^{-1})	227.77	192.19	63.54
V_{tpv}[b] (cm^3 g^{-1})	0.1251	0.1143	0.0861
d_{apz}[c] (nm)	2.20	2.38	6.16
Fe (wt.%)	0.52	2.09	8.02
La (wt.%)	BDL[d]	BDL	19.49

Calculated using the BET adsorption isotherm of nitrogen (77 K). [a]specific surface area. [b]total pore volume. [c]average pore size. [d]below detection limit

summarized in Table 1. Compared with the original B, the contents of Mg, Al, Ca, Fe, and La in MB and $La_{0.3}Fe_{0.1}$/MB were significantly increased with the introduction of binary metal, while the relative content of carbon on the surface of $La_{0.3}Fe_{0.1}$/MB was decreased, indicating that Fe and La were successfully anchored in $La_{0.3}Fe_{0.1}$/MB (Additional file 1: Table S2). The total La and Fe contents in $La_{0.3}Fe_{0.1}$/MB were 19.49% and 8.02%, respectively, which were lower than those of many La/Fe-based materials reported in the literature (Table 2). A previous study has shown that composites with lower La content may result in higher La utilization efficiency due

Table 2 Comparison of $La_{0.3}Fe_{0.1}$/MB with other newly developed adsorbents in the simultaneous of adsorption of phosphate

Adsorbents	Adsorption conditions				q_{max} (mg P g^{-1})	References
	P concentration (mg L^{-1})	Dosage (g L^{-1})	pH	T (℃)		
La-BC-5	2–50	2.0	3.0	25	23.52	Xu et al. (2020b)
La-MB	1–500	2.5	7.0	25	48.40	Zhong et al. (2020)
LMZ	25–400	2.0	n.a	25	52.52	Li et al. (2020)
La-doped magnetic rGO naocomposites	10–200	1.0	4–8	25–30	37.85	Rashidi Nodeh et al. (2017)
Fe_3O_4@SiO_2@La_2O_3	0–200	1.0	5–9	25	27.8	Lai et al. (2016)
La/Al pillaraed montmorillonite	5–50	2.5	5	25	13.02	Tian et al. (2009)
Magnetic biochar (fungal)	4–90	2.0	n.a	25	23.86	Jack et al. (2019)
La_2O_3/oak biochar	1–400	2.0	3-9	n.a	46.37	Wang et al. (2016)
$La_{0.3}Fe_{0.1}$/MB	1.75–300	2.0	7.4	28	52.12	This work

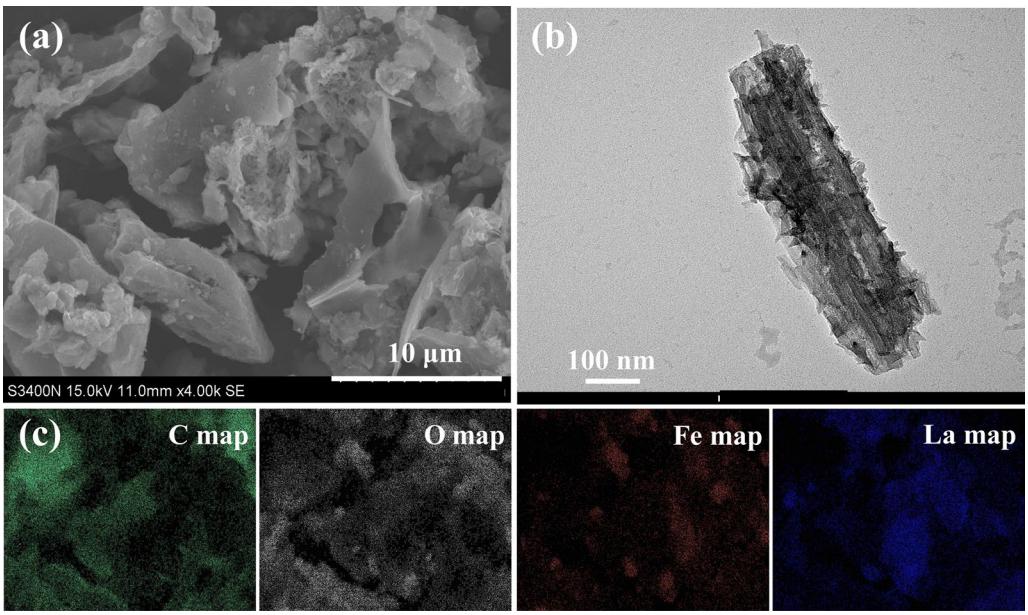

Fig. 1 SEM (**a**), TEM (**b**), EDS elemental mapping images (**c**) of $La_{0.3}Fe_{0.1}$/MB

to the uniform distribution of La and higher accessibility to phosphorus (Shi et al. 2019). Furthermore, the specific surface area of $La_{0.3}Fe_{0.1}$/MB decreased from 192.19–227.22 $m^2\ g^{-1}$ to 63.54 $m^2\ g^{-1}$, which was attributed to the loading of the impregnated iron and lanthanum on the surface of the material, as indicated by SEM–EDS results (Additional file 1: Fig. S2c and Fig. 1). A similar trend was also observed by Li et al. (2015) and Wang et al. (2016). Besides, the total pore volume of $La_{0.3}Fe_{0.1}$/MB decreased from 0.1143–0.1251 to 0.0861 $cm^3\ g^{-1}$, which was mainly due to the presence of iron/lanthanum adsorption sites on the surface or pores of MB and the filling of loaded particles inside (Xu et al. 2019). It has been reported by Yang et al. (2016) that the combined action of mineral and metal chlorides can improve the average pore diameter of BC (Yang et al. 2016). However, a slight increase in nanoparticle size was observed, and the adsorption average pore size potentially enhanced up to 2.20–2.38 nm to 6.16 nm for $La_{0.3}Fe_{0.1}$/MB indicating that $La_{0.3}Fe_{0.1}$/MB possesses a lesser surface area and pore space percent, except the higher pore size as compared with B and MB.

The morphologies of adsorbents were analyzed by SEM images, as shown in Additional file 1: Fig. S2. The raw B presented a relatively smooth and clean surface with mesoporous structure (Additional file 1: Fig. S2a), while M doping on the surface of biochar resulted in lamellar or bundled structures (Additional file 1: Fig. S2b). The EDS mapping confirmed that the immobilized Fe/La mainly resides in the cavities of the composite material.

Finally, the pore diameter of $La_{0.3}Fe_{0.1}$/MB showed a certain increase compared with B or MB. Particulate matter formation was observed and the material surface became rough and uneven (Additional file 1: Fig. S2c, d). In particular, a more irregular surface was observed for $La_{0.3}Fe_{0.1}$/MB, which can effectively improve the unit size of adsorbent (Fig. 1a). This appearance supports the lower specific surface area of $La_{0.3}Fe_{0.1}$/MB well (Table 1). As exhibited in the typical TEM images (Fig. 2b), the synthesized Lanthanum/iron oxide has a uniform size distribution.

The EDS spectra of all samples displayed prominent peaks for carbon, silicon, and oxygen (Additional file 1: Fig. S3). Furthermore, small amounts of Fe were present in the MB sample, confirming the M doping. More importantly, both iron and lanthanide were detected in LaFe/MB, and the corresponding peaks showed higher responsiveness. Peaks for Fe and La were also observed in the $Fe_{0.4}$/MB and $La_{0.4}$/MB adsorbents, respectively, confirming that La and Fe oxide were successfully anchored onto the adsorbents, which was in accordance with the SEM result. The elemental composition (wt.%) of the adsorbents is described in detail in Additional file 1: Table S2, which indicates strong Fe and La adsorption capacities. Metal oxides were mainly present on the biochar surface as determined by EDS. It is interesting to note that Fe and La loading was synergistic when La/Fe molar ratio was 0.3:0.1, compared with the loading of $La_{0.4}$/MB. The EDS mapping results confirmed that Fe and La were widely and abundantly distributed on the surface of porous granulated materials (Fig. 1c), thereby providing active adsorption sites for phosphate.

The chemical structure and functional groups of the samples were characterized by FTIR (Fig. 2a). The peaks observed at 3416–3441 cm^{-1} belonged to O–H stretching vibrations, the peak for C=O stretching vibrations of carbonyl or carboxyl groups was observed at around 1614–1634 cm^{-1}, while the peak at 1400 cm^{-1} was assigned to C=C stretching vibrations, respectively (Pezoti et al. 2016). The peak for Si–O–Mg bending

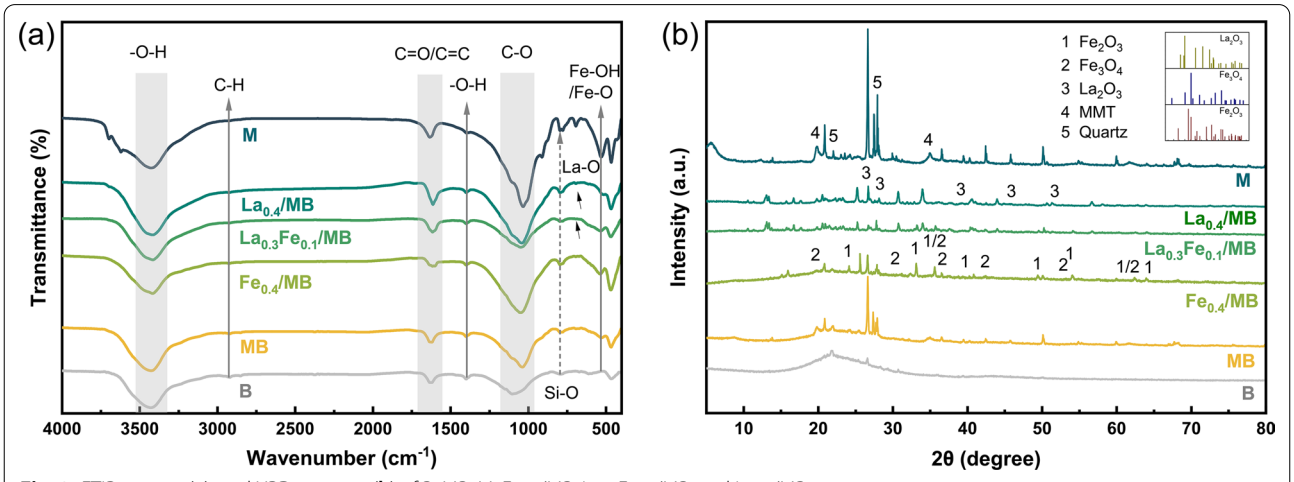

Fig. 2 FTIR spectra (**a**), and XRD patterns (**b**) of B, MB, M, $Fe_{0.4}$/MB, $La_{0.3}Fe_{0.1}$/MB, and $La_{0.4}$/MB

vibrations, present in all the adsorbent spectra, appeared at 693–664 cm^{-1}. The peak at 796–798 cm^{-1} can be attributed to Si–O stretching, which was significantly enhanced in MB, M, $Fe_{0.4}$/MB, $La_{0.3}Fe_{0.1}$/MB, and $La_{0.4}$/MB adsorbents, reflecting the effect of M on biochar substrate. Correspondingly, the C–O stretching vibration peak at around 1033–1049 cm^{-1} decreased when biochar was modified with both iron and lanthanum oxides. This may be due to the binding of iron/lanthanide to oxygen-containing groups in biochar (Chen et al. 2017). The peak at 530–536 cm^{-1} corresponded to the Fe–OH stretching vibration in $Fe_{0.4}$/MB and $La_{0.3}Fe_{0.1}$/MB (Li et al. 2008; Sun et al. 2019). Moreover, the La–O or La–OH stretching vibration at 674–664 cm^{-1} was more intense in $La_{0.4}$/MB and $La_{0.3}Fe_{0.1}$/MB (Fu et al. 2018; Zhang et al. 2011), showing that MB was successfully impregnated with Fe and La (Yin et al. 2017).

Figure 2b shows the XRD patterns of B, MB, M, $Fe_{0.4}$/MB, $La_{0.3}Fe_{0.1}$/MB, and $La_{0.4}$/MB. In the XRD patterns of samples containing MB, peak 4 (M, $2\theta = 19.6°$, 35.2°), peak 5 (quartz, $2\theta = 22.1°$, 27.9°), and a peak at $2\theta = 26.69°$ due to graphite were observed, suggesting that M was present in the formable porous granulated adsorbents and that the biochar structure was still retained (Zhu et al. 2020). Interestingly, the intensity of biochar peak decreased upon doping with iron and lanthanum oxides, indicating that the addition of metallic oxides decreased the relative amount of the main component of bone biochar. The XRD pattern of $Fe_{0.4}$/MB showed peaks corresponding to the typical XRD pattern of iron oxide. In particular, the diffraction peaks 1 and 2 observed at $2\theta = 20.88°$, 24.17°, 33.15°, 35.61°, 40.26°, 42.55°, 49.41°, 53.81°, and 62.52° can be ascribed to Fe_3O_4 and Fe_2O_3. This suggests that Fe can form iron oxide nanoparticles. The peaks that appeared at $2\theta = 26.63°$, 28.08°, 39.07°, and 51.43° for $La_{0.4}$/MB can be attributed to crystalline La_2O_3 (Goscianska et al. 2018; Qiu et al. 2017), which is consistent with the FTIR results. Comparing these diffraction patterns to that of $La_{0.3}Fe_{0.1}$/MB, similar characteristic diffraction peaks were observed for Fe_3O_4, Fe_2O_3, and La_2O_3, which suggests that iron and lanthanum oxides were successfully doped into MB. This was also confirmed by the EDS elemental mappings (Fig. 1c).

3.2 Macroscopic P adsorption performance and energy distribution

3.2.1 Adsorption kinetics

The rapid and effective removal of phosphate from wastewater is the key effect of adsorbents in practical applications. Initially, pseudo-first-order and pseudo-second-order kinetic models were employed to estimate the adsorption kinetics of phosphate onto $La_{0.3}Fe_{0.1}$/MB (Fig. 3a). The removal process of phosphate in aqueous solution was rapid within 30 min, and the adsorption capacity gradually reached equilibrium after approximately 5 h, indicating a fast kinetic process suitable for column-based practical phosphate removal. Associated sorption parameters are summarized in the table of Fig. 3a, which were obtained using the two model equations (details in Additional file 1: Text S1). Pseudo-second order model provided the best fit with the highest correlation coefficient (R^2) values for $La_{0.3}Fe_{0.1}$/MB (0.9751) compared to pseudo-first-order model (0.9158), suggesting chemi-sorption as the rate-controlling step for phosphate adsorption. Moreover, the adsorption data fitted ($q_{e,second}$ value was 40.41 mg g^{-1}) by the pseudo-second-order kinetic model were closer to the experimental values, indicating that the adsorption corresponded to monolayer chemisorption (Wang et al. 2020b). This result also confirmed the conclusion reported in the literature that there existed a strong chelation and complexation between phosphate and active sites of $La_{0.3}Fe_{0.1}$/MB (Chen et al. 2015; Shi et al. 2019).

In addition, the collected experimental data were fitted into the intra-particle diffusion model to further explain the adsorption mechanism and rate-limiting step. The plot of the intra-particle diffusion model of $La_{0.3}Fe_{0.1}$/MB for phosphate removal is shown in Additional file 1: Fig. S4, which was composed of three linear sections with distinct slopes, as also confirmed by some previous studies (Haris et al. 2022). The result implied that the adsorption mechanism entailed three nonlinear processes, including external diffusion which was related to surface diffusion, intra-particle diffusion where phosphate intercalated among the internal structure of the adsorbent layer, and adsorption on binding sites with chemical reaction. The adsorption rate constant (k_{pi}) values of the intra-particle diffusion models are listed in Table 3. The value of k_{p1} was larger than that of k_{p2} and k_{p3} (4.36, 1.00, and 0.06, respectively), indicating that intra-particle diffusion was the rate-controlling process (Shi et al. 2019). On the other hand, the line did not pass through the origin, instead, it had an intercept. This is in agreement with the findings of the pseudo-second- order model.

3.2.2 Isotherms and thermodynamic investigations

The adsorption isotherms of $La_{0.3}Fe_{0.1}$/MB at different phosphate concentrations are presented in Fig. 3b. $La_{0.3}Fe_{0.1}$/MB exhibited high phosphate adsorption capacity at low equilibrium concentration, suggesting a high affinity to phosphate that meets the requirement of advanced phosphate removal. Two commonly used models, the Langmuir and Freundlich models, were further used to fit the phosphate sorption data for $La_{0.3}Fe_{0.1}$/MB (details in Additional file 1: Text S2). The resulting best-fit parameters are listed in Additional

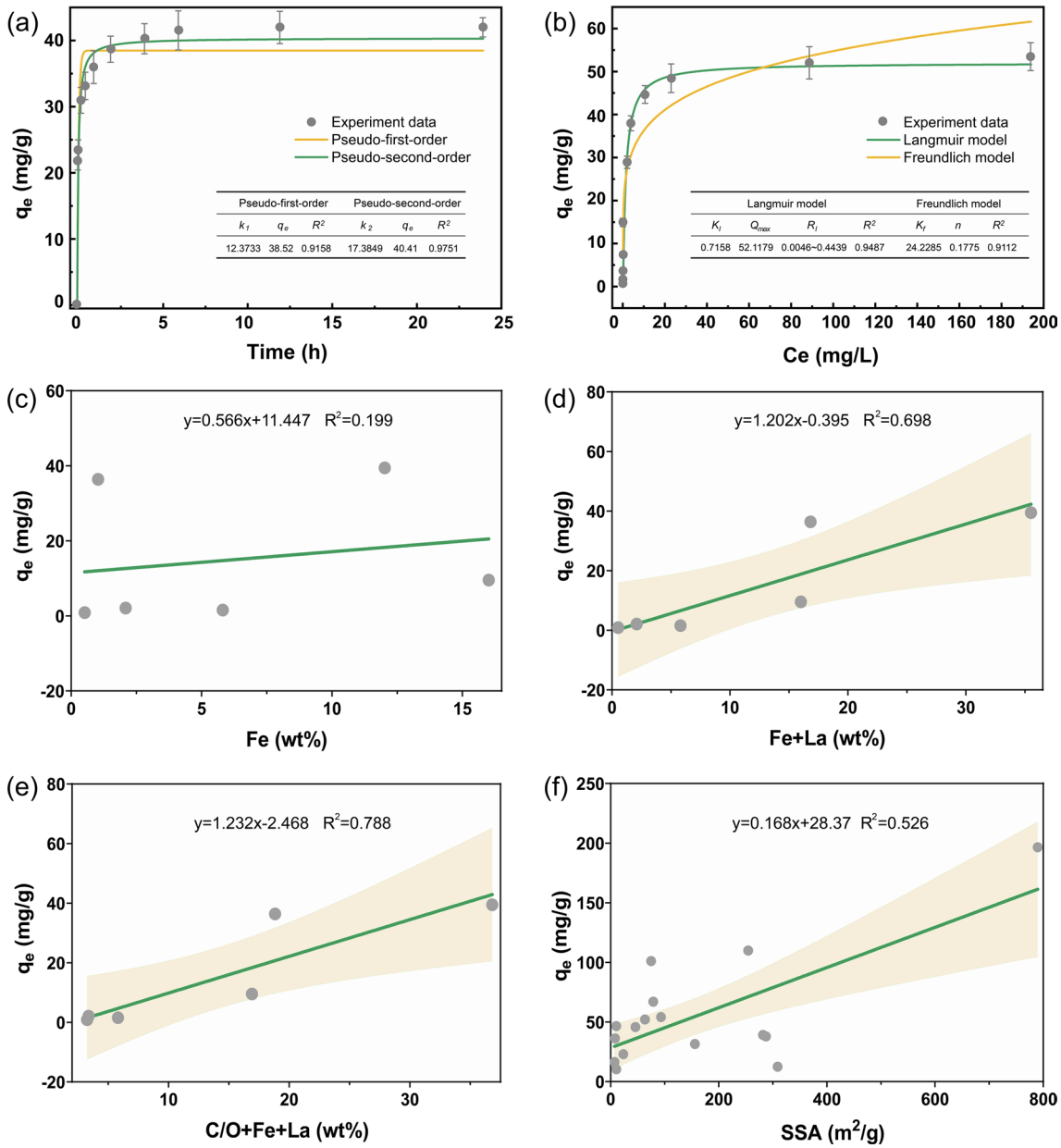

Fig. 3 Phosphate adsorption kinetics for $La_{0.3}Fe_{0.1}$/MB. Time dependence of the phosphate removal by $La_{0.3}Fe_{0.1}$/MB, using 50 mL of a 100 mg P L^{-1} solution, pH = 7.41, T = 298 K, 0.1 g adsorbent, and a total contact time of 6 h (**a**). Langmuir and Freundlich isotherms for $La_{0.3}Fe_{0.1}$/MB (**b**). Correlation between phosphate removal capacity and Fe, Fe + La, C/O + Fe + La (**c**–**e**), and specific surface area (SSA) of previous references (**f**)

Table 3 Intra-particle diffusion parameters for phosphate adsorption on $La_{0.3}Fe_{0.1}$/MB

	k_{p1}	C_1	R^2	k_{p2}	C_2	R^2	k_{p3}	C_3	R^2
$La_{0.3}Fe_{0.1}$/MB	4.36	14.05	0.9967	1.00	27.87	0.9868	0.06	39.97	0.5925

The unit of k_{pi} and C_i are g/(mg $min^{0.5}$), and mg g^{-1}, respectively

file 1: Fig. S3b. It can be concluded that the Langmuir model (R^2 = 0.9487) was more consistent with the adsorption isotherm data than the Freundlich model (R^2 = 0.9112). The better fit provided by the nonlinear Langmuir model indicated that phosphate adsorption was likely a monolayer molecular adsorption process,

and the adsorption process likely involved chemisorption rather than physisorption (Yu et al. 2009). According to the Langmuir equation, the maximum amount of phosphorus uptake by the $La_{0.3}Fe_{0.1}$/MB material was estimated to be 52.12 mg P g^{-1}, which was higher than most previously reported adsorbents (Table 2), indicating that $La_{0.3}Fe_{0.1}$/MB is a promising material for application as phosphate scavenger.

In addition, according to the Langmuir equation, the dimensionless separation factor R_l was calculated to be in the range of 0.0046 ~ 0.4439, indicating that the adsorption of phosphate ions on the surface of the adsorbent was favorable. Moreover, a larger value of R_l is more conducive to pollutant removal, which was confirmed by further studies. For further thermodynamic exploration, energy changes and spontaneity of the phosphate adsorption process (such as, entropy change (ΔS^0), free enthalpy change (ΔH^0), and energy change (ΔG^0)) were examined using Eqs. (1)–(3) (Tran et al. 2017):

$$\ln\left(K_d^0\right) = \frac{\Delta S^0}{R} - \frac{\Delta H^0}{RT} \quad (1)$$

$$\Delta G^0 = -RT \ln\left(K_d^0\right) \quad (2)$$

$$K_d = \frac{q_e}{C_e} \quad (3)$$

where ΔS^0, ΔH^0, and ΔG^0 are the standard entropy, enthalpy, and Gibbs free energy for the adsorption process, R is the ideal gas constant, T is the temperature (K), q_e is the adsorption uptake capacity of adsorbent for phosphate (mg g^{-1}), and C_e is the equilibrium concentration of phosphate (mg L^{-1}).

Using the plots of ln (q_e/C_e) versus q_e, the values of thermodynamic parameters were obtained. The values of ΔS^0 and ΔH^0 during the adsorption of phosphate were found to be 57.5454 J $(mol{\cdot}K)^{-1}$, and 1.1340 kJ mol^{-1}, respectively. The positive value of entropy and free enthalpy, affirming the endothermic nature with the rise in randomness at the solid–liquid interface during the phosphate adsorption process, implied an excellent binding affinity for phosphate ions (Zhang et al. 2021a). Furthermore, the value of ΔG^0 (− 17.32 kJ mol^{-1}) was found to be negative, indicating a spontaneous process in which the adsorption forces were strong enough to pass the energy barrier for phosphate uptake onto $La_{0.3}Fe_{0.1}$/MB.

3.2.3 Approximate site energy distribution analysis

Due to the complex surface topography of biochar, the adsorption sites on the surface of biochar are uneven, and the location energy of these adsorption sites is different (Wang et al. 2022). The area with high surface energy becomes the adsorption center of environmental pollutants, playing an important role in the adsorption process (Li et al. 2021).

Identifying site energy distribution (SED) of P sorption to $La_{0.3}Fe_{0.1}$/MB can provide useful information on sorption mechanisms (Wu et al. 2022). The site energy E^* of P sorption on $La_{0.3}Fe_{0.1}$/MB was calculated from isotherm modeling and Eq. (7) of Additional file 1: Text S3. As can be seen from Additional file 1: Fig. S5a, the E^* value decreased with increasing P phase sorption concentration Q_e. This indicates that P was preferentially adsorbed to the high-energy sorption site and then gradually diffused to low-energy sorption site due to the energy distribution on the surface of $La_{0.3}Fe_{0.1}$/MB unevenly. As reported in the previous literature (Li et al. 2021), the highly efficient phosphorus removal by a novel sludge-based magnetic gel bead (MCB_{13}) was analysis on approximate SED. The corresponding E^* value was 24.87 ~ 25.80 kJ mol^{-1}, but lower than $La_{0.3}Fe_{0.1}$/MB, which implied that a heterogeneous surface was detrimental to a higher value of E^* (Li et al. 2021). Additionally, under the same Q_e value, E^* on $La_{0.3}Fe_{0.1}$/MB was significantly higher than that of MCB_{13}, indicating it has much more high-energy adsorption sites (Liao et al. 2020). According to Eqs. (8) and (9) of Additional file 1: Text S3, the average site energies (E^*) was calculated in the range of the experimental concentrations. The average value of $E^*/\mu(E^*)$ of P to $La_{0.3}Fe_{0.1}$/MB was 30.64 kJ mol^{-1} based on Eq. (4). The $F(E^*)$ of $La_{0.3}Fe_{0.1}$/MB was much higher than that of MCB_{13}, indicating more high-energy and low-energy sites for P sorption to $La_{0.3}Fe_{0.1}$/MB, resulting in more available binding sites for P sorption.

The SED is depicted in Additional file 1: Fig. S5b, characterizing the site energy heterogeneity based on standard deviation $\sigma_e{}^*$ of SED. The $\sigma_e{}^*$ of SED was able to describe the adsorption site energy inhomogeneity (Shen et al. 2015), which could be quantified by Eqs. (5) and (6) as follows. According to Eq. (6), the $\sigma_e{}^*$ of SED for P to $La_{0.3}Fe_{0.1}$/MB was 4.32 kJ mol^{-1}. In constrast, the $\sigma_e{}^*$ was comparable between $La_{0.3}Fe_{0.1}$/MB and MCB_{13} (Li et al. 2021). The heterogeneous sorption sites originate from the defect structure, disordered arrangement, and grafting functional groups of carbonaceous materials, described with $\sigma_e{}^*$ (Shen et al. 2015; Wang et al. 2022). Overall, the Fe/La(hydr)oxides-loaded would introduce more high-energy sorption sites, thereby strengthening the interaction between P and $La_{0.3}Fe_{0.1}$/MB and increasing its removal.

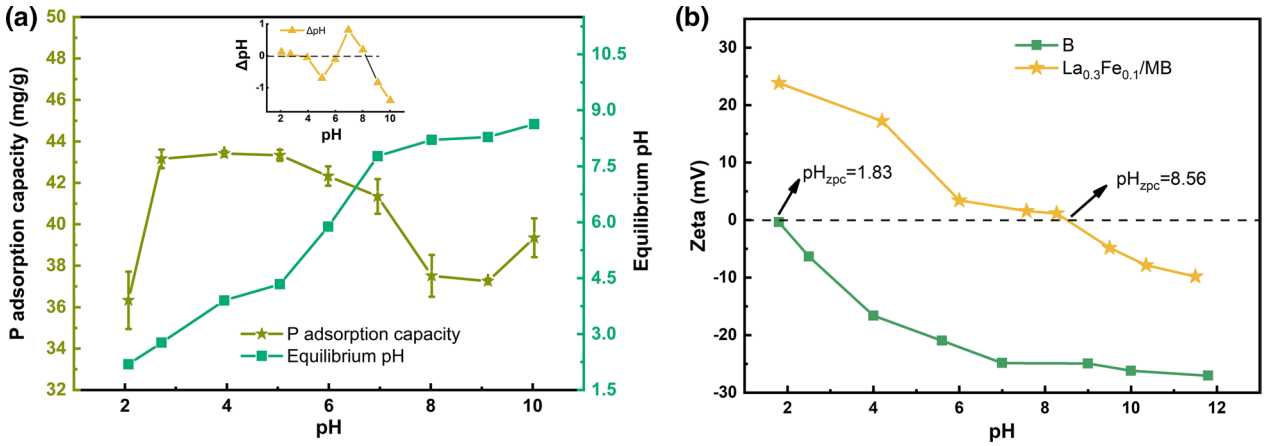

Fig. 4 Effects of pH and pH equilibria on phosphate adsorption (**a**), Zeta potential of $La_{0.3}Fe_{0.1}$/MB at different pH values (**b**)

$$\mu(E^*) = \frac{\int_a^b E^* F(E^*)\mathrm{d}E^*}{\int_a^b F(E^*)\mathrm{d}E^*} = \frac{\int_a^b E^* Q_{\max} \frac{K_L C_s \exp\left(-\frac{E^*}{RT}\right)}{RT\left(K_L C_s \exp\left(-\frac{E^*}{RT}\right)+1\right)^2}\mathrm{d}E^*}{\int_a^b Q_{\max} \frac{K_L C_s \exp\left(-\frac{E^*}{RT}\right)}{RT\left(K_L C_s \exp\left(-\frac{E^*}{RT}\right)+1\right)^2}\mathrm{d}E^*} \quad (4)$$

$$\mu\left(E^{*2}\right) = \frac{\int_a^b E^{*2} F(E^*)\mathrm{d}E^*}{\int_a^b F(E^*)\mathrm{d}E^*} = \frac{\int_a^b E^{*2} Q_{\max} \frac{K_L C_s \exp\left(-\frac{E^*}{RT}\right)}{RT\left(K_L C_s \exp\left(-\frac{E^*}{RT}\right)+1\right)^2}\mathrm{d}E^*}{\int_a^b Q_{\max} \frac{K_L C_s \exp\left(-\frac{E^*}{RT}\right)}{RT\left(K_L C_s \exp\left(-\frac{E^*}{RT}\right)+1\right)^2}\mathrm{d}E^*} \quad (5)$$

$$\sigma_e^* = \sqrt{\mu\left(E^{*2}\right) - \mu(E^*)^2} \quad (6)$$

3.2.4 Correlation between adsorbent properties and P adsorption

The correlations between the adsorption capacity and contents of Fe, Fe + La, and (C/O + Fe + La) in the adsorbents were analyzed. It was found that there was no correlation between the adsorption capacity and iron content, while the correlation increased significantly with the increase in La content ($R^2 = 0.698$), indicating that the loading of La greatly improved the adsorption capacity of the adsorbent. In addition, the loading of (C/O + Fe + La) further improved the correlation ($R^2 = 0.788$) which demonstrates that the C/O ratio also promoted the adsorption effect of adsorbents. Also, previous studies suggested that the introduction of iron can promote the uniform distribution of La/Fe bimetallic oxides in the composite's matrix. Subsequently, they can form colloidal or nanoscale oxides on the surface of the adsorbent, and then form mononuclear and polynuclear complexes with P through precipitation (Wang et al. 2016; Yao et al. 2013).

Given that the specific surface area (SSA) of adsorbents also affects the adsorption performance, a linear correlation was employed to estimate the relationship model (Fig. 3f). Although it has been widely reported that the specific surface area of the adsorbent contributes significantly to its adsorption performance (Mosa et al. 2018), the overall correlation between SSA and adsorption performance of $La_{0.3}Fe_{0.1}$/MB was found to be moderate ($R^2 = 0.5261$). Thus, combined with experimental conditions and results, it can be inferred that the uptake of phosphate by $La_{0.3}Fe_{0.1}$/MB was not mainly due to the high SSA of the adsorbent.

As can be seen from the data, $La_{0.3}Fe_{0.1}$/MB exhibited good phosphate removal performance with relatively low La content (Table 1), compared to other adsorbents doped with La or Fe reported in the literature (Table 2). Even at a lower concentration of adsorbent, the adsorption performance was maintained stably under the interference of co-existing competitive anions (Fig. 6a). Moreover, powder adsorbents or adsorbents with small-size particles are difficult to separate from aqueous solution, which affects their subsequent recovery and reuse in actual applications. Hence, it was found that there was no significant decrease in content of $La_{0.3}Fe_{0.1}$/MB for phosphate uptake, even compared with La modified zeolite (LMZ) reported by Li et al. (2020). More importantly, $La_{0.3}Fe_{0.1}$/MB adsorbent has formable porous spherical particles, which is conducive to its recovery and reuse.

3.3 Proposed adsorption mechanism

3.3.1 Influence of pH and zeta potential

pH also affects the protonation of phosphate in wastewater, the charge and stability of adsorbent, and especially, in the potential loss of metal oxide into solution (Xu et al. 2019). The relationship between solution pH and phosphate removal at pH 2–10 was studied (Fig. 4a). At pH 2–6, the amount of phosphate adsorbed by $La_{0.3}Fe_{0.1}$/MB first increased rapidly with the increase in pH and then decreased slowly until pH ~ 6. At pH values greater than ~ 6, phosphate adsorption decreased slightly with the increase in pH. On the whole, $La_{0.3}Fe_{0.1}$/MB showed a good tolerance to initial pH changes. In general, phosphate species (H_3PO_4, $H_2PO_4^-$, HPO_4^{2-}, and PO_4^{3-}) present in solution vary from acidic to basic with pH (Krishnan and Haridas 2008). When $pH < pH_{pzc}$ (8.56) (Fig. 4b), the $La_{0.3}Fe_{0.1}$/MB surface can be protonated ($\equiv Fe/La–OH + H^+ \leftrightarrow Fe/La–OH_2^+$). This leads to a strong electrostatic attraction between phosphate species present in solution and the relatively positively charged surface of the adsorbent, likely due to the formation of metal oxides on the surface. In addition, the amount of adsorbed phosphate decreased when pH exceeded pH_{pzc}, due to negative surface charges resulting from the release of hydroxyl groups during ligand exchange (Shi et al. 2019). Therefore, $La_{0.3}Fe_{0.1}$/MB can capture phosphate effectively over a wide pH range (3 ~ 10) without significant decrease in adsorption capacity.

Metal-loaded adsorbents can attract negatively charged phosphate anions (such as $H_2PO_4^-$ and HPO_4^{2-}) present in solution through electrostatic attraction at low pH value (Fig. 4b). At environmental pH values close to pH_{pzc}, the adsorption sites become weak, and the protonation of the surface decreases, leading to a charge that is close to zero. The positive values of ΔpH reflect the gradual increase in hydroxide content (Fig. 4a), which is mainly dependent on ligand exchange (Awual et al. 2011). When the solution pH continued to rise above 8.56, fierce repulsion occurred between negatively charged $La_{0.3}Fe_{0.1}$/MB and HPO_4^{2-}, resulting in a sharp decrease in P adsorption capacity. A high concentration of OH^- was unfavorable to ligand exchange and electrostatic attraction of phosphate by $La_{0.3}Fe_{0.1}$/MB, resulting in a downward trend of phosphate adsorption. Nevertheless, the adsorption capacity remained elevated over a range of pH of 9–10, mainly due to the complexation, which is another important mechanism in the adsorption process (Xu et al. 2019).

3.3.2 Raman, XPS, and XRD analyses

Furthermore, the phosphate adsorption mechanisms of $La_{0.3}Fe_{0.1}$/MB were investigated using a combination of Raman, XPS, and XRD analyses. Figure 5a and b show the Raman spectra of $La_{0.3}Fe_{0.1}$/MB pre and post P adsorption. The characteristic peaks belonging to the D and G bands appeared around 1588 cm^{-1} and 1363 cm^{-1}, respectively. The strong G-peak of the in-plane vibration mode confirmed the graphite carbon in $La_{0.3}Fe_{0.1}$/MB, while the strong D-peak of the ring breathing vibration reflected the existence of a large number of pores and edge defects (Yap et al. 2019). The D/G intensity ratio (obtained by taking the ratio of the total peak areas in the 1300–1400 cm^{-1} and 1500–1600 cm^{-1} ranges) of $La_{0.3}Fe_{0.1}$/MB decreased from 11,427/3819 to 7996/2890 after phosphate adsorption (Fig. 5a, b). Based on a two-peak fitting model, the peak intensity ratio (I_D/I_G) of the D and G bands declined by 6.54% (from 1.0096 to 0.9436), suggesting that the graphitization of $La_{0.3}Fe_{0.1}$/MB was enhanced and the ordered sp^2 carbon content in the structure increased after phosphate adsorption. This may contribute to the improvement of the strength of $La_{0.3}Fe_{0.1}$/MB after phosphate adsorption (Fig. 6c). The formation of a more ordered interface structure after phosphate uptake further implies that precipitation might also be an important mechanism of $La_{0.3}Fe_{0.1}$/MB for phosphate removal.

From the total survey scans of $La_{0.3}Fe_{0.1}$/MB (Fig. 5), the O 1 s spectra could be separated into three overlapping peaks at 531.2, 532.26, and 533.23 eV, corresponding to M–O (oxygen bonded to a metal), M–OH (hydroxyl bonded to a metal), and adsorbed water (H_2O), respectively. After phosphate adsorption, the relative areas of M–O peaks increased from 23.41% to 49.48%, confirming that $La_{0.3}Fe_{0.1}$/MB can replace hydroxyl groups with P through ligand exchange, which plays a key role in phosphate absorption (Shi et al. 2019). This result may be due to the combination of P with O–La and O–Fe to form La–O–P and Fe–O–P (Fu et al. 2018). Since this value (1.48) lies between 0.5 and 2, monodentate, bidentate mononuclear, and bidentate binuclear inner-complexes may be formed during the adsorption process (He et al. 2016). The relative content of M–OH decreased from 47.42% to 31.97% after P adsorption, demonstrating the possible exchange of –OH with P to form inner-complex (Fang et al. 2018; Xu et al. 2020b). The P_{2p} spectra contained an obvious peak at ~ 133.35 eV, while similar to the reference samples of $LaPO_4 \cdot xH_2O$ (132.85 eV) and $FePO_4 \cdot {}_2H_2O$ (133.68 eV), which further confirmed the assumption that M–O–P bonds were formed (Fu et al. 2018; He et al. 2017). This finding was consistent with the work of Wang et al. (2016). As can be seen, some H_3PO_4 analog was observed which caused by the adsorption of P by $LaPO_4$ through hydrogen bonding. This phenomenon was also been observed in other reports (Yao et al. 2013). It is, therefore, demondtrated that the precipitation was the mechanism for P removal using $La_{0.3}Fe_{0.1}$/MB.

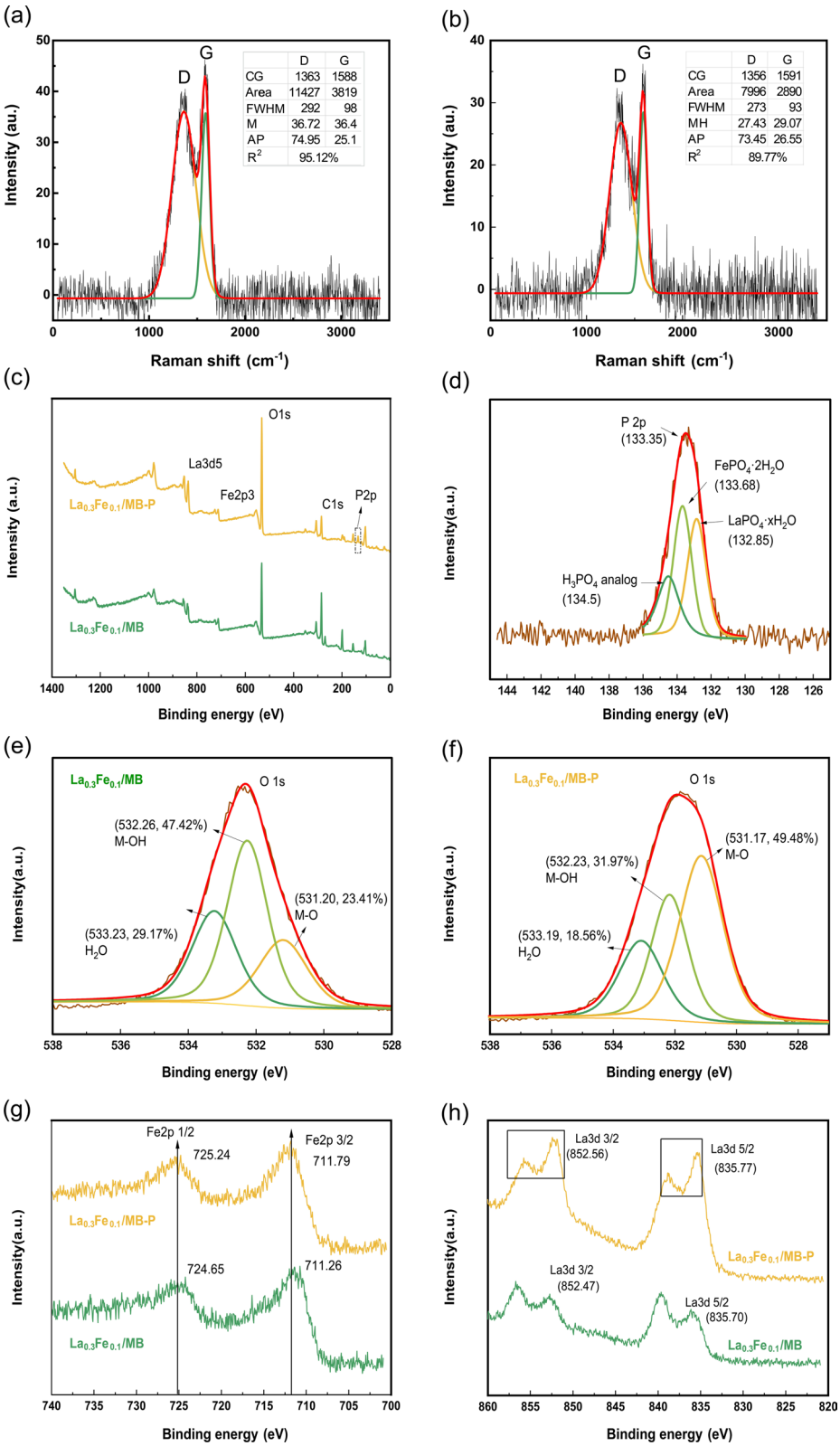

Fig. 5 Raman mapping analysis of $La_{0.3}Fe_{0.1}$/MB before (**a**) and after P adsorption (**b**); X-ray photoelectron spectra of $La_{0.3}Fe_{0.1}$/MB before and after P adsorption: survey scan (**c**); P 2p region (**d**); O_{1s} region (**e** and **f**); Fe_{2p} region (**g**) and La_{3d} region (**h**)

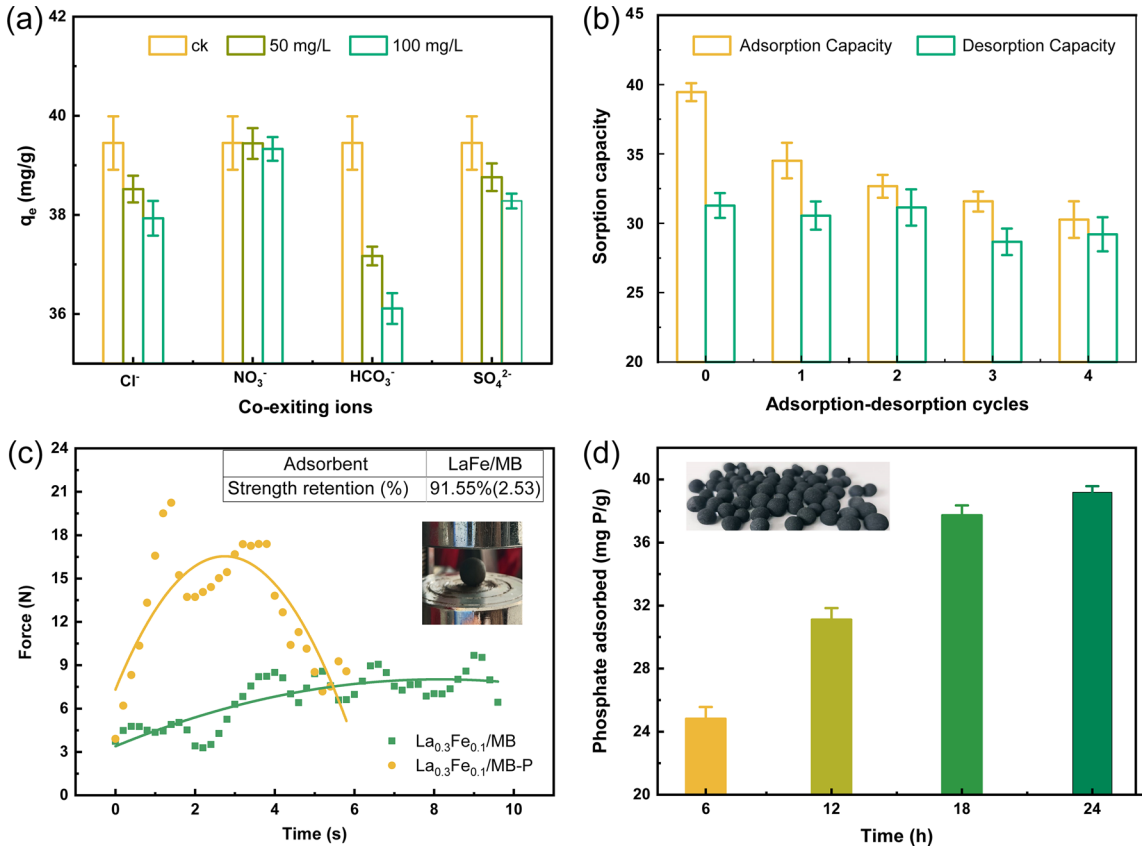

Fig. 6 Effects of co-existing ions on phosphate adsorption by $La_{0.3}Fe_{0.1}$/MB at pH = 7.05 (**a**), dsorption-desorption cycle experiments of phosphate (**b**), force changes of adsorbent before and after adsorption (4 mm in diameter) (**c**), and Phosphate adsorption capacity of wastewater (**d**)

In addition, the Fe $_{2p1/2}$, and Fe $_{2p3/2}$ spectra showed a slight shift in peaks from 724.65 and 711.26 eV to 725.24 and 711.79 eV, and this shift agreed well with the formation of Fe–O–P bonding (Fang et al. 2018), implying the possible involvement of iron during phosphate uptake. Moreover, the peaks associated with La $_{3d5/2}$ and La $_{3d3/2}$ located at 835.70 eV/839.46 eV, 852.47 eV/856.46 eV were found for $La_{0.3}Fe_{0.1}$/MB in the XPS spectra, while the binding energies shifted to 835.77 eV (La $_{3d5/2}$) and 852.56 eV (La $_{3d3/2}$) after the capture of P, which was likely due to a possible transfer of electrons leading to the formation of $LaPO_4{\cdot}xH_2O$ after adsorption (Wu et al. 2017; Xu et al. 2019). The XRD pattern of $La_{0.3}Fe_{0.1}$/MB further successfully verified the formation of La–P with weak typical peaks of $LaPO_4$ (JCPDS 04-0635), based on previous investigation (Shi et al. 2019), as shown in Additional file 1: Fig. S6. These results demonstrated that phosphate was removed via the precipitation of Fe/La and phosphate ions (Li et al. 2016), which confirmed that Fe and La were involved in phosphate adsorption.

To summarize, electrostatic attraction, ligand exchange, and surface precipitation were collectively involved in the removal of P by $La_{0.3}Fe_{0.1}$/MB. Moreover, the adsorption of phosphate ions on the surface of the adsorbent was favorable and exhibited an excellent binding affinity according to the isotherms and thermodynamic investigations.

3.4 Practical application potential

3.4.1 Effect of co-existing ions on phosphate adsorption

There is a variety of co-existing ions such as Cl^-, NO_3^-, SO_4^{2-}, and HCO_3^- in actual wastewater, which may affect the P removal efficiency of adsorbent through Coulomb force (Chen et al. 2016), but also due to other mechanisms (Chen et al. 2015; Shi et al. 2019). It has previously been reported that HCO_3^- anion can compete with phosphate by forming inner-sphere complexes reducing P removal efficiency (Chen et al. 2015; Shi et al. 2019). In a further set of experiments, the effects of interfering co-existing ions on phosphate adsorption onto $La_{0.3}Fe_{0.1}$/MB at the concentrations of 50 and 100 mg P L^{-1} were assessed with the result shown in Fig. 6a. As observed, NO_3^- was found to possess a negligible effect on P adsorption by $La_{0.3}Fe_{0.1}$/MB, closely followed by

SO_4^{2-}, and Cl^- which exhibited insignificant effects on P uptake with above 97.64% and 96.15% of phosphate removal occurring at both co-existing ions concentrations, respectively. In relative terms, the adsorption capacity decreased in the range examined, with 94.22% and 91.53% of P uptake in the presence of HCO_3^- at 50 and 100 mg L^{-1}, respectively. It was evident that HCO_3^- had some influence on P binding onto $La_{0.3}Fe_{0.1}$/MB, especially at a relatively higher concentration, maybe due to the higher affinity of La-based adsorbents for HCO_3^- than that for PO_4^{3-} (Qiu et al. 2017). Overall, data analysis showed that common anions in water had an insignificant influence on the adsorption capacity of $La_{0.3}Fe_{0.1}$/MB for P removal. In other words, these results suggested $La_{0.3}Fe_{0.1}$/MB was suitable for real wastewater implementation owing to its outstanding attraction for P in the case of ions interference.

3.4.2 Consecutive regeneration

Reusability of adsorbent is important for evaluating the practicability and cost-effectiveness of wastewater treatment processes and materials. The regeneration test was then carried out to evaluate the applicability of $La_{0.3}Fe_{0.1}$/MB from economical perspective. As seen from Fig. 4a, the decrease in adsorption capacity at higher pH region indicated that highly alkaline pH may cause the desorption of P from $La_{0.3}Fe_{0.1}$/MB. The adsorbent after P saturation was subjected to regeneration with 0.1 mol L^{-1} NaOH solution. The results showed that after four adsorption–desorption cycles, $La_{0.3}Fe_{0.1}$/MB experienced 87.48% bind of P during the 1st cycle and more than 76.23% of adsorption efficiency was maintained after four cycles as shown in Fig. 6b. The slight decrease in phosphorus adsorption may be due to permanent filling of the active site by subsequent uptake cycles (Zhang et al. 2021a). In addition, the desorption capacity remained at 29.21 mg g^{-1} after four cycles, confirming the $La_{0.3}Fe_{0.1}$/MB P-recovery potential even after reuse. This result further emphasizes the outstanding practical applicability of $La_{0.3}Fe_{0.1}$/MB in the field of adsorption, making it suitable for the purification of phosphate-containing wastewater.

3.4.3 Actual river water phosphorus adsorption and strength retention

The pond water of Jiangsu Academy of Agricultural Sciences was taken as the test sample to evaluate the actual application potential of the adsorbent (basic parameters, as well as the specific sampling point and time, are detailed in Additional file 1: Text S4). To this sample, a certain amount of phosphate was added to adjust the concentration of phosphate to 30 mg P L^{-1}. The strength retention rate, pressure resistance, and phosphorus adsorption capacity of $La_{0.3}Fe_{0.1}$/MB were measured, respectively, at the end of 24 h of adsorption (Fig. 6c and d). It can be seen that after the practical wastewater treatment operation, the adsorbent still showed a high strength retention rate up to 91.55%, and its resistance to pressure change increased from 6.21 N to 16.54 N. This was due to the complexation reaction and crystallization, which can be beneficial to the efficient recovery of phosphorus resources. Compared with simulated water, the phosphorus adsorption equilibrium of adsorbent in actual wastewater was delayed from 3 to 18 h, but the adsorption capacity did not change much, indicating that it has excellent potential in practical engineering application.

Meanwhile, metal leaching of $La_{0.3}Fe_{0.1}$/MB in actual wastewater was tracked (Additional file 1: Text S5), which was adapted according to Shen et al. (2022). From Additional file 1: Table S3, it could be seen that given actual wastewater contained a high amount of Fe, while La was not detectable. When $La_{0.3}Fe_{0.1}$/MB was added, the concentration of La was increased with the prolonged leaching time until equilibrium after the third day, reaching a maximum of 0.006 mg L^{-1}, which was below the standard limit of European Union. It is worth noting that, due to the rich specific surface area and functional groups of $La_{0.3}Fe_{0.1}$/MB, which has a certain adsorption capacity for Fe, and little Fe leached, the trial group had slightly lower Fe concentration than the control group on day 0. However, the Fe concentration of the control group was generally balanced on day 5th, mainly because the suspended particles in the water settled. The Fe concentration increased from 0.0613 mg L^{-1} to 0.0807 mg L^{-1} on the first day, indicating partial iron leaching from $La_{0.3}Fe_{0.1}$/MB. Then it tended to balance and the concentration decreased to 0.0440 mg L^{-1}, still slightly larger than the control group, indicating partial Fe leaching from $La_{0.3}Fe_{0.1}$/MB into wastewater. And by the seventh day, the Fe concentration was increased by 0.0023 mg L^{-1} (Δ_{Fe}), with Fe values far lower than the standard limit value (0.03 mg L^{-1}) of supplementary items for centralized drinking water surface water source by Chinese National Standard GB 3838-2002 (Environmental Quality Standards for Surface Water). These results demonstrate that the presence of metal (Fe and La) oxides in biochar has a low potential environmental risk to water bodies.

4 Conclusion

Herein, a formable porous biochar (LaFe/MB) was synthesized via in situ preloading of lanthanide/iron oxide and montmorillonite nanoparticles on the biochar surface, followed by co-pyrolysis. Phosphate adsorption performance of this composite was then evaluated. The results showed that the molar ratio of Fe and La significantly influenced the phosphate adsorption performance.

The adsorption kinetic data could be fitted well by the pseudo-second-order model and Langmuir isotherm, indicating that LaFe/MB had a high adsorption efficiency for phosphate. The presence of most co-existing ions had little impact on phosphate adsorption. LaFe/MB was characterized by FTIR, XRD, SEM/EDX, zeta potential measurements, and XPS analyses. The results demonstrated that electrostatic attraction, ligand exchange, and surface precipitation played major roles in phosphate removal with maximum equilibrium adsorption capacity (Langmuir model) of 52.12 mg P g^{-1}. Negative $\Delta G°$, positive $\Delta H°$, and $\Delta S°$ values indicated that the adsorption of phosphate onto LaFe/MB was a spontaneous and endothermic process. The strength retention rate of LaFe/MB was as high as 91.6% in the actual wastewater application, and the resistance to pressure of LaFe/MB before and after adsorption increased from 6.21 N to 16.54 N, which was conducive to the recovery of biochar. This work demonstrated that LaFe/MB is a promising adsorbent for both enhanced relief of eutrophication and efficient recovery of phosphorus strategic resources. Future experiments will evaluate the LaFe/MB adsorbents' potential for recovering phosphate from multiple actual wastewater scenarios, environmental impact assessment, techno-economic investigation, and life cycle analysis of formable porous biochar is required for future performance validation.

Supplementary Information

The online version contains supplementary material available at https://doi.org/10.1007/s42773-022-00177-8.

Additional file 1. Supplementary texts, figures and tables. **Text S1**. Mathematical equations and corresponding curve fitting model formulas of adsorption kinetics. **Text S2**. Langmuir and Freundlich isotherm models of adsorption isotherms. **Text S3**. Adsorption site energy distribution. **Text S4**. Basic parameters of the pond water, as well as the specific sampling point and time. **Text S5**. Leaching experiment of Fe and La from $La_{0.3}Fe_{0.1}$/MB in actual water. **Fig. S1**. Phosphate adsorption capacities of different adsorbents in a solution with an initial concentration of 100 mg P L^{-1}. **Fig. S2**. Scanning electron microscopy (SEM) images of (a) B, (b) MB, (c) $Fe_{0.4}$/MB, (d) $La_{0.4}$/MB. **Fig. S3**. Energy dispersive spectra (EDS) of B, MB, M, $Fe_{0.4}$/MB, $La_{0.3}Fe_{0.1}$/MB, and $La_{0.4}$/MB. **Fig. S4**. Phosphate adsorption fitted data of $La_{0.3}Fe_{0.1}$/MB conducted by intra-particle diffusion model results. **Fig. S5**. Langmuir model based-site energy on phosphate solid-phase sorption (a), Langmuir model based-site energy distribution of phosphate sorption on $La_{0.3}Fe_{0.1}$/MB (b). **Fig. S6**. XRD patterns of $La_{0.3}Fe_{0.1}$/MB after phosphate adsorption. **Table S1**. Preparation conditions used to obtain the different formable porous granulated LaFe/MB adsorbents. **Table S2**. Surface elemental composition (wt.%) of adsorbents. **Table S3**. Leaching concentration of Fe and La from $La_{0.3}Fe_{0.1}$/MB in actual water.

Acknowledgements
The authors want to thank Professor Bingcai Pan, deputy dean of School of Environmental Sciences and director of the Center for Environmental Nanotenology of Nanjing University. Thanks to Professor Linzhang Yang (co-supervisor), academic leader of agricultural non-point source pollution control innovation team, for his leading role of scientific research. Thanks to Professor Charles Hunter (supervisor) of the University of KwaZulu-Natal (Pietermaritzburg Campus) for his inspiration and support, and Professor Hongying Huang for his constant supports and encouragement. The authors also acknowledge Jiangsu Collaborative Innovation Center for Solid Organic Waste Resource Utilization, and Key Laboratory of Saline-Alkali Soil Improvement and Utilization (Coastal Saline-Alkali Lands), Ministry of Agriculture and Rural Affairs, PR, China.

Author contributions
ES: Conceptualization, Methodology, Data management, Writing—original draft. YZ: Methodology, Data curation, Writing—review and editing. QX: Investigation, and Funding acquisition. HL: Writing and review. PQ: Methodology, Data curation. CY: Methodology and Data curation. BW: Review and editing, mathematical model validation. YF: Methodology, Validation, Data curation, Review and editing, Funding acquisition. HH: Validation, Review and editing. CH: Supervision, Formal analysis, Validation, Data curation, Review and editing. LY: Co-supervision, Conceptualization, Resources, Validation, Data curation. All authors read and approved the final manuscript.

Funding
The research was funded by National Key Research and Development Program of China (2021YFD1700805), National Natural Science Foundation of China (41807132; 22078136, 41877090), and the Jiangsu Province Agricultural Independent Innovation Fund (CX(19)2003).

Availability of data and materials
The data and material used in this manuscript will be made available by the authors upon request.

Declarations

Ethics approval and consent to participate
Not applicable.

Competing interests
The authors unanimously decleare that they have no known competing financial interests or personal relationships that might influence the work reported here.

Author details
[1]Key Laboratory of Saline-Alkali Soil Improvement and Utilization (Coastal Saline-Alkali Lands), Ministry of Agriculture and Rural Affairs, Jiangsu Collaborative Innovation Center for Solid Organic Waste Resource Utilization, Institute of Agricultural Resources and Environment, Jiangsu Academy of Agricultural Sciences, Nanjing 210014, China. [2]School of Life Sciences, College of Agriculture, Engineering and Science, University of KwaZulu-Natal (Pietermaritzburg Campus), Private Bag X01, Scottsville 3209, Republic of South Africa. [3]State Key Laboratory of Pollution Control and Resource Reuse, School of the Environment, Nanjing University, Nanjing 210023, China. [4]Institute of Germplasm Resources and Biotechnology, Jiangsu Academy of Agricultural Sciences, Nanjing 210014, China. [5]Jiangsu Key Laboratory of Chemical Pollution Control and Resources Reuse, School of Environmental and Biological Engineering, Nanjing University of Science and Technology, Nanjing 210094, China.

Received: 11 March 2022 Accepted: 27 August 2022
Published online: 14 September 2022

References

Ahmed S, Lo IMC (2020) Phosphate removal from river water using a highly efficient magnetically recyclable Fe_3O_4/$La(OH)_3$ nanocomposite. Chemosphere 261:128118. https://doi.org/10.1016/j.chemosphere.2020.128118

Ai T, Jiang XJ, Liu QY et al (2019) Daptomycin adsorption on magnetic ultra-fine wood-based biochars from water: kinetics, isotherms, and mechanism studies. Biores Technol 273:8–15. https://doi.org/10.1016/j.biortech.2018.10.039

An X, Wu Z, Yu J et al (2020) High-efficiency reclaiming phosphate from an aqueous solution by bentonite modified biochars: a slow release fertilizer with a precise rate regulation. ACS Sustain Chem Eng 8:6090–6099. https://doi.org/10.1021/acssuschemeng.0c01112

Arif M, Liu G, Yousaf B et al (2021) Synthesis, characteristics and mechanistic insight into the clays and clay minerals-biochar surface interactions for

contaminants removal-a review. J Clean Prod 310:127548. https://doi.org/10.1016/j.jclepro.2021.127548
Arola K, Mänttäri M, Kallioinen M (2021) Two-stage nanofiltration for purification of membrane bioreactor treated municipal wastewater—minimization of concentrate volume and simultaneous recovery of phosphorus. Sep Purif Technol 256:117255. https://doi.org/10.1016/j.seppur.2020.117255
Awual MR, Jyo A, Ihara T et al (2011) Enhanced trace phosphate removal from water by zirconium(IV) loaded fibrous adsorbent. Water Res 45:4592–4600. https://doi.org/10.1016/j.watres.2011.06.009
Bacelo H, Pintor AMA, Santos SCR et al (2020) Performance and prospects of different adsorbents for phosphorus uptake and recovery from water. Chem Eng J 381:122566. https://doi.org/10.1016/j.cej.2019.122566
Banu HT, Karthikeyan P, Meenakshi S (2018) Lanthanum (III) encapsulated chitosan-montmorillonite composite for the adsorptive removal of phosphate ions from aqueous solution. Int J Biol Macromol 112:284–293. https://doi.org/10.1016/j.ijbiomac.2018.01.138
Cakmak EK, Hartl M, Kisser J et al (2022) Phosphorus mining from eutrophic marine environment towards a blue economy: the role of bio-based applications. Water Res 219:118505. https://doi.org/10.1016/j.watres.2022.118505
Caravelli AH, De Gregorio C, Zaritzky NE (2012) Effect of operating conditions on the chemical phosphorus removal using ferric chloride by evaluating orthophosphate precipitation and sedimentation of formed precipitates in batch and continuous systems. Chem Eng J 209:469–477. https://doi.org/10.1016/j.cej.2012.08.039
Carter MC, KilduffWeber JWJ (1995) Site energy distribution analysis of preloaded adsorbents. Environ Sci Technol 29:1773–1780
Cerofoline GF (1974) Localized adsorption on heterogeneous surfaces. Thin Solid Films 23:129–152
Chen L, Zhao X, Pan BC et al (2015) Preferable removal of phosphate from water using hydrous zirconium oxide-based nanocomposite of high stability. J Hazard Mater 284:35–42. https://doi.org/10.1016/j.jhazmat.2014.10.048
Chen M, Huo C, Li Y et al (2016) Selective adsorption and efficient removal of phosphate from aqueous medium with graphene-lanthanum composite. ACS Sustain Chem Eng 4:1296–1302. https://doi.org/10.1021/acssuschemeng.5b01324
Chen L, Chen XL, Zhou CH et al (2017) Environmental-friendly montmorillonite-biochar composites: facile production and tunable adsorption-release of ammonium and phosphate. J Clean Prod 156:648–659. https://doi.org/10.1016/j.jclepro.2017.04.050
Chen W, Meng J, Han X et al (2019) Past, present, and future of biochar. Biochar 1:75–87. https://doi.org/10.1007/s42773-019-00008-3
Delaney P, McManamon C, Hanrahan JP et al (2011) Development of chemically engineered porous metal oxides for phosphate removal. J Hazard Mater 185:382–391. https://doi.org/10.1016/j.jhazmat.2010.08.128
Fang L, Liu R, Li J et al (2018) Magnetite/Lanthanum hydroxide for phosphate sequestration and recovery from lake and the attenuation effects of sediment particles. Water Res 130:243–254. https://doi.org/10.1016/j.watres.2017.12.008
Feng Y, Lu H, Liu Y et al (2017) Nano-cerium oxide functionalized biochar for phosphate retention: preparation, optimization and rice paddy application. Chemosphere 185:816–825. https://doi.org/10.1016/j.chemosphere.2017.07.107
Fletcher AJ, Smith MA, Heinemeyer A et al (2013) Production factors controlling the physical characteristics of biochar derived from phytoremediation willow for agricultural applications. BioEnergy Res 7:371–380. https://doi.org/10.1007/s12155-013-9380-x
Fu HY, Yang YX, Zhu RL et al (2018) Superior adsorption of phosphate by ferrihydrite-coated and lanthanum decorated magnetite. J Colloid Interface Sci 530:704–713. https://doi.org/10.1016/j.jcis.2018.07.025
Goscianska J, Ptaszkowska-Koniarz M, Frankowski M et al (2018) Removal of phosphate from water by lanthanum-modified zeolites obtained from fly ash. J Colloid Interface Sci 513:72–81. https://doi.org/10.1016/j.jcis.2017.11.003
Haris M, Usman M, Su F et al (2022) Programmable synthesis of exfoliated biochar nanosheets for selective and highly efficient adsorption of thallium. Chem Eng J 434:134842. https://doi.org/10.1016/j.cej.2022.134842
He YH, Lin H, Dong YB et al (2016) Simultaneous removal of ammonium and phosphate by alkaline-activated and lanthanum-impregnated zeolite. Chemosphere 164:387–395. https://doi.org/10.1016/j.chemosphere.2016.08.110
He YH, Lin H, Dong YB et al (2017) Preferable adsorption of phosphate using lanthanum-incorporated porous zeolite: characteristics and mechanism. Appl Surf Sci 426:995–1004. https://doi.org/10.1016/j.apsusc.2017.07.272
Huang X, Wei D, Zhang XW et al (2019) Synthesis of amino-functionalized magnetic aerobic granular sludge-biochar for Pb(II) removal: adsorption performance and mechanism studies. Sci Total Environ 685:681–689. https://doi.org/10.1016/j.scitotenv.2019.05.429
Huang Y, He Y, Zhang H et al (2022) Selective adsorption behavior and mechanism of phosphate in water by different lanthanum modified biochar. J Environ Chem Eng 10:107476. https://doi.org/10.1016/j.jece.2022.107476
Islam MS, Zhang Y, Dong S et al (2017) Dynamics of microbial community structure and nutrient removal from an innovative side-stream enhanced biological phosphorus removal process. J Environ Manage 198:300–307. https://doi.org/10.1016/j.jenvman.2017.04.074
Jack J, Huggins TM, Huang YP et al (2019) Production of magnetic biochar from waste-derived fungal biomass for phosphorus removal and recovery. J Clean Prod 224:100–106. https://doi.org/10.1016/j.jclepro.2019.03.120
Jung KW, Ahn KH (2016) Fabrication of porosity-enhanced MgO/biochar for removal of phosphate from aqueous solution: application of a novel combined electrochemical modification method. Bioresour Technol 200:1029–1032. https://doi.org/10.1016/j.biortech.2015.10.008
Jung KW, Jeong TU, Kang HJ et al (2016) Characteristics of biochar derived from marine macroalgae and fabrication of granular biochar by entrapment in calcium-alginate beads for phosphate removal from aqueous solution. Biores Technol 211:108–116. https://doi.org/10.1016/j.biortech.2016.03.066
Krishnan KA, Haridas A (2008) Removal of phosphate from aqueous solutions and sewage using natural and surface modified coir pith. J Hazard Mater 152:527–535. https://doi.org/10.1016/j.jhazmat.2007.07.015
Kumar M, Xiong X, Wan Z et al (2020a) Ball milling as a mechanochemical technology for fabrication of novel biochar nanomaterials. Bioresour Technol 312:123613. https://doi.org/10.1016/j.biortech.2020.123613
Kumar M, Xiong XN, Wan ZH et al (2020b) Ball milling as a mechanochemical technology for fabrication of novel biochar nanomaterials. Biores Technol 312:123613. https://doi.org/10.1016/j.biortech.2020.123613
Lai L, Xie Q, Chi L et al (2016) Adsorption of phosphate from water by easily separable Fe_3O_4@SiO_2 core/shell magnetic nanoparticles functionalized with hydrous lanthanum oxide. J Colloid Interface Sci 465:76–82. https://doi.org/10.1016/j.jcis.2015.11.043
Lazaratou CV, Vayenas DV, Papoulis D (2020) The role of clays, clay minerals and clay-based materials for nitrate removal from water systems: a review. Appl Clay Sci 185:105377. https://doi.org/10.1016/j.clay.2019.105377
Le Corre KS, Valsami-Jones E, Hobbs P et al (2009) Phosphorus recovery from wastewater by struvite crystallization: a review. Crit Rev Environ Sci Technol 39:433–477. https://doi.org/10.1080/10643380701640573
Li GY, Jiang YR, Huang KL et al (2008) Preparation and properties of magnetic Fe_3O_4-chitosan nanoparticles. J Alloy Compd 466:451–456. https://doi.org/10.1016/j.jallcom.2007.11.100
Li G, Shen B, Li F et al (2015) Elemental mercury removal using biochar pyrolyzed from municipal solid waste. Fuel Process Technol 133:43–50. https://doi.org/10.1016/j.fuproc.2014.12.042
Li RH, Wang JJ, Zhou BY et al (2016) Recovery of phosphate from aqueous solution by magnesium oxide decorated magnetic biochar and its potential as phosphate-based fertilizer substitute. Biores Technol 215:209–214. https://doi.org/10.1016/j.biortech.2016.02.125
Li X, Kuang Y, Chen J et al (2020) Competitive adsorption of phosphate and dissolved organic carbon on lanthanum modified zeolite. J Colloid Interface Sci 574:197–206. https://doi.org/10.1016/j.jcis.2020.04.050
Li H, Zhao Y, Xiao Z et al (2021) Analysis on approximate site energy distribution and adsorption behaviors unveils reasons for highly efficient phosphorus removal by a novel sludge-based magnetic gel bead. Chem Eng J 422:130028. https://doi.org/10.1016/j.cej.2021.130028
Liao P, Li B, Xie L et al (2020) Immobilization of Cr(VI) on engineered silicate nanoparticles: microscopic mechanisms and site energy distribution. J Hazard Mater 383:121145. https://doi.org/10.1016/j.jhazmat.2019.121145
Liu L, Zhang C, Chen S et al (2022) Phosphate adsorption characteristics of $La(OH)_3$-modified, canna-derived biochar. Chemosphere 286:131773. https://doi.org/10.1016/j.chemosphere.2021.131773

Melia PM, Busquets R, Hooda PS et al (2019) Driving forces and barriers in the removal of phosphorus from water using crop residue, wood and sewage sludge derived biochars. Sci Total Environ 675:623–631. https://doi.org/10.1016/j.scitotenv.2019.04.232

Mohan D, Sarswat A, Ok YS et al (2014) Organic and inorganic contaminants removal from water with biochar, a renewable, low cost and sustainable adsorbent—a critical review. Biores Technol 160:191–202. https://doi.org/10.1016/j.biortech.2014.01.120

Mosa A, El-Ghamry A, Tolba M (2018) Functionalized biochar derived from heavy metal rich feedstock: phosphate recovery and reusing the exhausted biochar as an enriched soil amendment. Chemosphere 198:351–363. https://doi.org/10.1016/j.chemosphere.2018.01.113

Ngatia LW, Hsieh YP, Nemours D et al (2017) Potential phosphorus eutrophication mitigation strategy: biochar carbon composition, thermal stability and pH influence phosphorus sorption. Chemosphere 180:201–211. https://doi.org/10.1016/j.chemosphere.2017.04.012

Panahi HKS, Dehhaghi M, Ok YS et al (2020) A comprehensive review of engineered biochar: production, characteristics, and environmental applications. J Clean Prod 270:122462. https://doi.org/10.1016/j.jclepro.2020.122462

Pezoti O, Cazetta AL, Bedin KC et al (2016) NaOH-activated carbon of high surface area produced from guava seeds as a high-efficiency adsorbent for amoxicillin removal: Kinetic, isotherm and thermodynamic studies. Chem Eng J 288:778–788. https://doi.org/10.1016/j.cej.2015.12.042

Qiu H, Liang C, Yu JH et al (2017) Preferable phosphate sequestration by nano-La(III) (hydr)oxides modified wheat straw with excellent properties in regeneration. Chem Eng J 315:345–354. https://doi.org/10.1016/j.cej.2017.01.043

Rajapaksha AU, Chen SS, Tsang DCW et al (2016) Engineered/designer biochar for contaminant removal/immobilization from soil and water: potential and implication of biochar modification. Chemosphere 148:276–291. https://doi.org/10.1016/j.chemosphere.2016.01.043

Rashidi Nodeh H, Sereshti H, Zamiri Afsharian E et al (2017) Enhanced removal of phosphate and nitrate ions from aqueous media using nanosized lanthanum hydrous doped on magnetic graphene nanocomposite. J Environ Manage 197:265–274. https://doi.org/10.1016/j.jenvman.2017.04.004

Reguyal F, Sarmah AK (2018) Site energy distribution analysis and influence of Fe_3O_4 nanoparticles on sulfamethoxazole sorption in aqueous solution by magnetic pine sawdust biochar. Environ Pollut 233:510–519. https://doi.org/10.1016/j.envpol.2017.09.076

Rong X, Xie M, Kong LS et al (2019) The magnetic biochar derived from banana peels as a persulfate activator for organic contaminants degradation. Chem Eng J 372:294–303. https://doi.org/10.1016/j.cej.2019.04.135

Shen X, Guo X, Zhang M et al (2015) Sorption mechanisms of organic compounds by carbonaceous materials: site energy distribution consideration. Environ Sci Technol 49:4894–4902. https://doi.org/10.1021/es506034e

Shen X, Meng H, Shen Y et al (2022) A comprehensive assessment on bioavailability, leaching characteristics and potential risk of polycyclic aromatic hydrocarbons in biochars produced by a continuous pyrolysis system. Chemosphere 287:132116. https://doi.org/10.1016/j.chemosphere.2021.132116

Shi WM, Fu YW, Jiang W et al (2019) Enhanced phosphate removal by zeolite loaded with Mg-Al-La ternary (hydr)oxides from aqueous solutions: performance and mechanism. Chem Eng J 357:33–44. https://doi.org/10.1016/j.cej.2018.08.003

Song BQ, Chen M, Zhao L et al (2019) Physicochemical property and colloidal stability of micron- and nano-particle biochar derived from a variety of feedstock sources. Sci Total Environ 661:685–695. https://doi.org/10.1016/j.scitotenv.2019.01.193

Su Y, Cui H, Li Q et al (2013) Strong adsorption of phosphate by amorphous zirconium oxide nanoparticles. Water Res 47:5018–5026. https://doi.org/10.1016/j.watres.2013.05.044

Sun YQ, Yu IKM, Tsang DCW et al (2019) Multifunctional iron-biochar composites for the removal of potentially toxic elements, inherent cations, and hetero-chloride from hydraulic fracturing wastewater. Environ Int 124:521–532. https://doi.org/10.1016/j.envint.2019.01.047

Tian S, Jiang P, Ning P et al (2009) Enhanced adsorption removal of phosphate from water by mixed lanthanum/aluminum pillared montmorillonite. Chem Eng J 151:141–148. https://doi.org/10.1016/j.cej.2009.02.006

Tomczyk A, Sokolowska Z, Boguta P (2020) Biochar physicochemical properties: pyrolysis temperature and feedstock kind effects. Rev Environ Sci Bio-Technol 19:191–215. https://doi.org/10.1007/s11157-020-09523-3

Tran HN, You SJ, Hosseini-Bandegharaei A et al (2017) Mistakes and inconsistencies regarding adsorption of contaminants from aqueous solutions: a critical review. Water Res 120:88–116. https://doi.org/10.1016/j.watres.2017.04.014

Vieira RM, Vilela PB, Becegato VA et al (2018) Chitosan-based hydrogel and chitosan/acid-activated montmorillonite composite hydrogel for the adsorption and removal of Pb^{+2} and Ni^{+2} ions accommodated in aqueous solutions. J Environ Chem Eng 6:2713–2723. https://doi.org/10.1016/j.jece.2018.04.018

Viglasova E, Galambos M, Dankova Z et al (2018) Production, characterization and adsorption studies of bamboo-based biochar/montmorillonite composite for nitrate removal. Waste Manage 79:385–394. https://doi.org/10.1016/j.wasman.2018.08.005

Wang ZH, Shen DK, Shen F et al (2016) Phosphate adsorption on lanthanum loaded biochar. Chemosphere 150:1–7. https://doi.org/10.1016/j.chemosphere.2016.02.004

Wang B, Gao B, Fang J (2017) Recent advances in engineered biochar productions and applications. Crit Rev Environ Sci Technol 47:2158–2207. https://doi.org/10.1080/10643389.2017.1418580

Wang K, Sun YB, Tang JC et al (2020a) Aqueous Cr(VI) removal by a novel ball milled Fe-0-biochar composite: role of biochar electron transfer capacity under high pyrolysis temperature. Chemosphere 241:125044. https://doi.org/10.1016/j.chemosphere.2019.125044

Wang L, Wang JY, Yan W et al (2020b) $MgFe_2O_4$-biochar based lanthanum alginate beads for advanced phosphate removal. Chem Eng J 387:123305. https://doi.org/10.1016/j.cej.2019.123305

Wang B, Shang C, Xie H et al (2022) Unraveling natural aging-induced properties change of sludge-derived hydrochar and enhanced cadmium sorption site heterogeneity. Biochar 4:34. https://doi.org/10.1007/s42773-022-00159-w

Weber K, Quicker P (2018) Properties of biochar. Fuel 217:240–261. https://doi.org/10.1016/j.fuel.2017.12.054

Wu BL, Fang LP, Fortner JD et al (2017) Highly efficient and selective phosphate removal from wastewater by magnetically recoverable $La(OH)_3$/Fe_3O_4 nanocomposites. Water Res 126:179–188. https://doi.org/10.1016/j.watres.2017.09.034

Wu P, Ata-Ul-Karim ST, Singh BP et al (2019) A scientometric review of biochar research in the past 20 years (1998–2018). Biochar 1:23–43. https://doi.org/10.1007/s42773-019-00002-9

Wu P, Wang Z, Wang H et al (2020) Visualizing the emerging trends of biochar research and applications in 2019: a scientometric analysis and review. Biochar 2:135–150. https://doi.org/10.1007/s42773-020-00055-1

Wu L, Zhao X, Bi E (2022) Predicting the effect of dissolved humic acid on sorption of benzotriazole to biochar. Biochar 4:15. https://doi.org/10.1007/s42773-022-00134-5

Xu Q, Chen Z, Wu Z et al (2019) Novel lanthanum doped biochars derived from lignocellulosic wastes for efficient phosphate removal and regeneration. Bioresour Technol 289:121600. https://doi.org/10.1016/j.biortech.2019.121600

Xu CY, Li QR, Geng ZC et al (2020a) Surface properties and suspension stability of low-temperature pyrolyzed biochar nanoparticles: effects of solution chemistry and feedstock sources. Chemosphere 259:127510. https://doi.org/10.1016/j.chemosphere.2020.127510

Xu X, Cheng Y, Wu X et al (2020b) La(III)-bentonite/chitosan composite: a new type adsorbent for rapid removal of phosphate from water bodies. Appl Clay Sci 190:105547. https://doi.org/10.1016/j.clay.2020.105547

Yang F, Zhao L, Gao B et al (2016) The interfacial behavior between biochar and soil minerals and its effect on biochar stability. Environ Sci Technol 50:2264–2271. https://doi.org/10.1021/acs.est.5b03656

Yao Y, Gao B, Chen JJ et al (2013) Engineered biochar reclaiming phosphate from aqueous solutions: mechanisms and potential application as a slow-release fertilizer. Environ Sci Technol 47:8700–8708. https://doi.org/10.1021/es4012977

Yao Y, Gao B, Fang J et al (2014) Characterization and environmental applications of clay–biochar composites. Chem Eng J 242:136–143. https://doi.org/10.1016/j.cej.2013.12.062

Yap PL, Kabiri S, Tran DNH et al (2019) Multifunctional binding chemistry on modified graphene composite for selective and highly efficient

adsorption of mercury. ACS Appl Mater Interfaces 11:6350–6362. https://doi.org/10.1021/acsami.8b17131
Yin HB, Kong M, Gu XH et al (2017) Removal of arsenic from water by porous charred granulated attapulgite-supported hydrated iron oxide in bath and column modes. J Clean Prod 166:88–97. https://doi.org/10.1016/j.jclepro.2017.08.026
Yu Q, Zhang RQ, Deng SB et al (2009) Sorption of perfluorooctane sulfonate and perfluorooctanoate on activated carbons and resin: Kinetic and isotherm study. Water Res 43:1150–1158. https://doi.org/10.1016/j.watres.2008.12.001
Zhang L, Wan LH, Chang N et al (2011) Removal of phosphate from water by activated carbon fiber loaded with lanthanum oxide. J Hazard Mater 190:848–855. https://doi.org/10.1016/j.jhazmat.2011.04.021
Zhang M, Song G, Gelardi DL et al (2020) Evaluating biochar and its modifications for the removal of ammonium, nitrate, and phosphate in water. Water Res 186:116303. https://doi.org/10.1016/j.watres.2020.116303
Zhang Y, Akindolie MS, Tian X et al (2021a) Enhanced phosphate scavenging with effective recovery by magnetic porous biochar supported $La(OH)_3$: kinetics, isotherms, mechanisms and applications for water and real wastewater. Bioresour Technol 319:124232. https://doi.org/10.1016/j.biortech.2020.124232
Zhang YY, Ahmed S, Zheng ZX et al (2021b) Validation of pilot-scale phosphate polishing removal from surface water by lanthanum-based polymeric nanocomposite. Chem Eng J 412:128630. https://doi.org/10.1016/j.cej.2021.128630
Zhong Z, Lu X, Yan R et al (2020) Phosphate sequestration by magnetic La-impregnated bentonite granules: a combined experimental and DFT study. Sci Total Environ 738:139636. https://doi.org/10.1016/j.scitotenv.2020.139636
Zhu SH, Wang S, Yang X et al (2020) Green sustainable and highly efficient hematite nanoparticles modified biochar-clay granular composite for Cr(VI) removal and related mechanism. J Clean Prod 276:123009. https://doi.org/10.1016/j.jclepro.2020.123009